Identification of HSC/MPP expansion units in fetal liver by spatiotemporal transcriptomics

Suwei Gao[1, 2, 5#], Qiang Shi[3#], Yifan Zhang[1, 2, 5], Guixian Liang[1, 2, 5], Zhixin Kang[1, 2, 5], Baofeng Huang[1, 2,5], Dongyuan Ma[1, 2], Lu Wang[4], Jianwei Jiao[2, 5, 6], Xiangdong Fang[2, 5, 7, 8], Cheng-Ran Xu[9], Longqi Liu[10, 11], Xun Xu[10, 12], Berthold Gottgens[13], Cheng Li[3*], and Feng Liu[1, 2, 5, 14*]

[1] State Key Laboratory of Membrane Biology, Institute of Zoology, Chinese Academy of Sciences, Beijing 100101, China

[2] Institute for Stem Cell and Regeneration, Chinese Academy of Sciences, Beijing 100101, China

[3] School of Life Sciences, Center for Bioinformatics, Center for Statistical Science, Peking University, Beijing 100871, China

[4] State Key Laboratory of Experimental Hematology, Institute of Hematology and Blood Diseases Hospital, Chinese Academy of Medical Sciences and Peking Union Medical College, Tianjin 300020, China

[5] University of Chinese Academy of Sciences, Beijing 100049, China

[6] State Key Laboratory of Stem Cell and Reproductive Biology, Institute of Zoology, Chinese Academy of Sciences, Beijing 100101, China

[7] CAS Key Laboratory of Genome Science & Information, Beijing Institute of Genomics, Chinese Academy of Sciences/ China National Center for Bioinformation, Beijing 100101, China

[8] Beijing Key Laboratory of Genome and Precision Medicine Technologies, Beijing 100101, China

[9] Ministry of Education Key Laboratory of Cell Proliferation and Differentiation, College of Life Sciences, Peking-Tsinghua Center for Life Sciences, Peking University, Beijing 100871,

China.

[10] BGI-ShenZhen, Shenzhen 518103, China.

[11] Shenzhen Bay Laboratory, Shenzhen 518000, China.

[12] Guangdong Provincial Key Laboratory of Genome Read and Write, Shenzhen 518120, China

[13] Department of Haematology, Wellcome-Medical Research Council Cambridge Stem Cell Institute, University of Cambridge, Cambridge, CB2 0AW, UK

[14] Lead Contact

[#] These authors contributed equally to this work

[*] Corresponding authors

Feng Liu, liuf@ioz.ac.cn; **Cheng Li**, cheng_li@pku.edu.cn

ABSTRACT

Limited knowledge of underlying cellular and molecular mechanisms of hematopoietic stem cell and multipotent progenitor (HSC/MPP) expansion within their native niche has impeded the application of stem-cell based therapies for hematological malignances. Here, we constructed a spatiotemporal transcriptome map of mouse fetal liver (FL) as a platform for hypothesis generation and subsequent experimental validation of novel regulatory mechanisms. Single-cell transcriptomics revealed three transcriptionally heterogeneous HSC/MPP subsets, in which CD93-enriched subset exhibited enhanced stem cell properties. Moreover, by employing the integrative analysis of single-cell and spatial transcriptomics, we identified novel HSC/MPP 'pocket-like' units (HSC PLUS), composed of niche cells (hepatoblasts, stromal cells, endothelial cells, and macrophages), and enriched with growth factors. Unexpectedly, macrophages showed a 11-fold enrichment in the HSC PLUS. Functionally, macrophage-HSC/MPP co-culture assay and small molecule screening, respectively, validated the supportive role of macrophages and growth factors (MDK, PTN, and IGFBP5) in HSC/MPP expansion. Finally, cross-species analysis and functional validation showed conserved cell-cell interactions and expansion mechanisms but divergent transcriptome signatures between mouse and human FL HSCs/MPPs. Taken together, these results provide an essential resource for HSC/MPP development in FL, with implications for functional HSC/MPP expansion *ex vivo*.

INTRODUCTION

In mammals, hematopoietic stem cells and multipotent progenitors (HSCs/MPPs), occupying the top of hematopoietic hierarchy, display multilineage differentiation and self-renewal abilities[1]. Studying HSC/MPP expansion holds great promise for regenerative medicine[2], and significant efforts have been devoted to fulfilling long-term *ex vivo* HSC/MPP expansion via genetic manipulation or optimization of culture conditions[3,4]. Nevertheless, in current *ex vivo* HSC/MPP expansion culture, the key challenge is how to maintain the stem cell properties; therefore, a comprehensive understanding of HSC/MPP expansion within their native niche *in vivo* is required.

Highly vascularized fetal liver (FL) serves as the transitory developmental site for various sources of hematopoietic cells (HCs). In mice, the early wave of HCs colonizing the FL contains yolk sac erythro-myeloid progenitors (EMP), which will generate erythroid-myeloid lineages, including macrophages[5,6]. Subsequently, aorta-gonad-mesonephros (AGM)-derived HSCs migrate into the FL for maturation, expansion, and differentiation[7-9]. Mounting evidence in mice demonstrates that FL structural niche cells, including endothelial cells (ECs), stromal cells, and hepatoblasts, interact with HSCs/MPPs via diverse growth factors, cytokines, and chemokines[10-13]. These aforementioned findings preferentially focus on the effects of certain niche cell types or specific signaling molecules on HSC/MPP expansion. However, the mechanisms underlying the complex interplay among HSCs/MPPs and distinct niche cells, and the systematic regulatory network for HSC/MPP expansion remain elusive.

Single-cell RNA sequencing (scRNA-seq) represents a powerful tool to map cell atlas of single organ or multiple organs[14,15]. However, the weakness of scRNA-seq is the loss of

information about the cell-type spatial organization within intact organs. To expand our understanding of the spatial organization of diverse cell types in an unbiased manner, spatial transcriptomics (ST) has been developed[16]. Here, to examine the organ-wide regulatory mechanisms of HSC/MPP expansion, we employed scRNA-seq and ST (including 10x Visium and Stereo-seq) to generate a spatiotemporal transcriptome map of mouse FL. With this map, we revealed the transcriptional heterogeneity of HSCs/MPPs, with a focus on a $CD93^{+}$ subset exhibiting enhanced stem cell properties. We also decoded the architectural and molecular bases of HSC/MPP expansion. Furthermore, cross-species comparative analysis identified both conserved and divergent cellular and molecular events between mouse and human FL hematopoiesis. The map is accessible through an intuitive and interactive web portal at http://liulab.ioz.ac.cn/fetal_liver/. Together, our study reports a spatiotemporal transcriptomics blueprint for understanding HSC/MPP development in FL and provides valuable insights into HSC/MPP expansion *ex vivo*.

RESULTS

Single-cell transcriptomics atlas of the developing mouse FL

Previous studies have shown that FL-colonized HSCs/MPPs acquire definitive signatures from E11.5 to E12.5[17], followed by exhibiting expansion and differentiation characteristics from E12.5 to E14.5[7,18]. To resolve the temporal dynamics of HSCs/MPPs and their niche at the transcriptomics level, we employed 10x Genomics to generate a single-cell resolution cell atlas of the developing FL at one-day intervals between E11.5 and E14.5 (Fig. 1a). To enrich HCs and ECs, we used fluorescence-activated cell sorting (FACS) at these time points to separately sort HCs, ECs, and non-hematopoietic/non-endothelial cells from the FL, and subsequently pooled them together in certain ratios for sequencing (see MATERIALS AND METHODS; Supplementary information, Fig. S1a, b). In total, 32,449 single cells were retained for Uniform Manifold Approximation and Projection (UMAP)[19] analysis after quality control (Fig. 1b; Supplementary information, Fig. S1c, d). Based on the signature gene expression, we annotated 21 cell clusters (Fig. 1c; Supplementary information, Fig. S1e, f and Table S1), including 18 HC clusters and three structural niche cell clusters, and found that their fractions were dynamically correlated with the developmental stages (Supplementary information, Fig. S1g). Specifically, HSCs/MPPs [cluster (C) 1, C2, and C3] exhibited high expression levels of stem cell signature genes *Mycn*, *Hlf*, and *Mecom*[20,21]. Lymphoid progenitors (C4) were marked by *Ccr9*, *Il7r*, and *Flt3*. Myeloid progenitors (C6) were characterized by the expression of *Mpo*, *Spi1*, and *Ccl9*[22]. Three structural niche cell clusters consisted of C19 ECs (*Lyve1*, *Kdr*, and *Pecam1*), C20 stromal cells (*Pdgfra*, *Alcam*, and *Ncam1*), and C21 hepatoblasts (*Afp*, *Alb*, and *Ttr*) (Fig. 1c; Supplementary information, Fig. S1f).

The development of HSCs/MPPs and FL structural niche cells is tightly regulated by dynamic transcriptional programs[13,17]. Accordingly, we focused on the transcriptional dynamics of HSCs/MPPs and structural niche cells. Analysis of differentially expressed genes (DEGs) was performed among four stages, and gene ontology (GO) analysis of DEGs in HSCs/MPPs identified that lymphoid program and immune response were enriched at E11.5 and E12.5, and hematopoietic development and mitotic cell cycle regulation were enriched at E13.5 and E14.5 (Fig. 1d, e). This suggests that the transcriptional dynamics of HSCs/MPPs in the developing FL underlies the maturation and expansion of HSCs/MPPs, which is consistent with previous reports[17,23]. Moreover, GO analysis showed that mitotic cell cycle regulation and cell growth were also enriched in different types of structural niche cells, indicating a global increase in cell number and size to accommodate the FL expansion. Specifically, ECs exhibited vasculature sprouting at E11.5 and E12.5, and cell-cell adherent junctions at E13.5 and E14.5 (Supplementary information, Fig. S2a, b), representing a gradual formation of the FL vasculature. For the stromal cells, ribonucleoprotein biogenesis and RNA translation were enriched at E11.5 and E12.5, and extracellular structure organization and growth factor production were enriched at E13.5 and E14.5 (Supplementary information, Fig. S2c, d), suggesting that stromal cells provide structural support and signaling interaction for tissue development. GO analysis of hepatoblasts showed that ribosome biogenesis was enriched at E11.5 and E12.5, and metabolic regulation was enriched at E13.5 and E14.5 (Supplementary information, Fig. S2e, f). Taken together, we generated the first fully-annotated single-cell resolution atlas of mouse FL, shown in a freely-available website (Supplementary information, Video S1), to gain a comprehensive understanding of cellular composition dynamics, cell type-

specific gene expression and stage-specific biological functions of both HSCs/MPPs and structural niche cells during FL development.

CD93-enriched HSCs/MPPs exhibit enhanced stem cell properties

To further dissect the transcriptome features of HSCs/MPPs, we focused on HSC/MPP1-3 clusters and explored the underlying differences among them. GO and DEG analyses indicated enrichment of hematopoietic regulation and differentiation, active translation processes, and cell cycle regulation in HSC/MPP1-3, respectively (Fig. 2a, b). In HSC/MPP1, the expression of *Mycn*, *Mecom*, and *Hlf* was enriched; in HSC/MPP2, metabolic and lineage-specific genes were highly expressed; and in HSC/MPP3, cell cycle related genes showed highly enriched expression (Fig. 2b, c). To further evaluate the stem cell properties of heterogeneous HSCs/MPPs, we calculated hscScore as previously reported[24], and found that the highest score was seen in HSC/MPP1 (Fig. 2d; Supplementary information, Table S2); meanwhile, trajectory analysis[25] among HSC/MPP subsets and downstream myeloid and lymphoid progenitors revealed that HSC/MPP1 occupied the top of hematopoietic hierarchy (Fig. 2e). Overall, these results indicate that HSC/MPP1 exhibit the most robust stem cell transcriptome feature, compared to HSC/MPP2-3.

To enrich HSC/MPP1 cells, we identified a cell-surface marker gene, *Cd93*, the expression of which was upregulated in HSC/MPP1 relative to HSC/MPP2-3 (Fig. 2f). Given that *Cd93* (also known as *AA4.1*) has been shown to be expressed in hematopoietic progenitors[26-28], we asked whether the combination of CD93 and other HSC/MPP markers, such as Lineage$^-$ Sca-1$^+$c-Kit$^+$ (LSK), Flt3$^-$LSK, and CD150$^+$CD48$^-$LSK (SLAM-LSK)[29,30], can further purify

HSCs/MPPs with robust stem cell properties. Flow cytometry analysis indicated that LSK (Supplementary information, Fig. S3a), SLAM-LSK (Supplementary information, Fig. S3c), and Flt3$^-$LSK (Supplementary information, Fig. S3e) cells at E14.5 could be clearly divided into CD93$^+$ and CD93$^-$ groups. Colony-forming unit (CFU) analysis showed that CD93$^+$ cells (CD93$^+$LSK, CD93$^+$Flt3$^-$LSK, and CD93$^+$SLAM-LSK) exhibited a higher colony-forming ability than CD93$^-$ cells (Supplementary information, Fig. S3b, d, f). Among them, CD93$^+$SLAM-LSK cells displayed the most robust colony-forming ability of CFU-granulocyte, erythroid, macrophage, and megakaryocyte (CFU-GEMM) than other HSC/MPP groups (Supplementary information, Fig. S3d). To evaluate the engraftment ability of HSCs/MPPs purified by CD93$^+$SLAM-LSK combination, we performed primary and secondary transplantation assays. The results showed that E14.5 CD93$^+$SLAM-LSK cells exhibited higher reconstitution and self-renewal abilities than CD93$^-$ SLAM-LSK cells (Fig. 2g-j). Moreover, to determine whether the CD93 can enrich HSCs/MPPs from heterogeneous LSK cells[31,32], we performed primary transplantation assay and the results showed that E14.5 CD93$^+$LSK cells exhibited a higher short-term (8 weeks) and long-term (16 weeks) reconstitution abilities than LSK cells (Supplementary information, Fig. S3g); meanwhile, we also found that both E14.5 CD93^{High}- and CD93^{Mid} LSK cells exhibited higher colony-forming and short-term (4 weeks) reconstitution abilities than the CD93^{Low} LSK cells (Supplementary information, Fig. S3h, i). Furthermore, to reveal the functional role of CD93 in FL HSC/MPP development, we characterized the E14.5 FL HSC/MPP phenotype of CD93 genetic mutants (CD93 KO), whose knockout efficiency was validated at protein level (Supplementary information, Fig. S4a). Consequently, although the absolute number of whole FL cells and the proportion of

undifferentiated Lineage$^-$ cells had no obvious change in the CD93 KO embryos (Supplementary information, Fig. S4b, c), the proportion of HSCs/MPPs (LSK cells and SLAM-LSK cells) was decreased in the CD93 KO embryos (Supplementary information, Fig. S4d-f). Taken together, CD93 is not only a surface marker for characterizing HSC/MPP heterogeneity, but also functionally required for FL HSC/MPP development.

Integration of scRNA-seq and ST decodes cell-cell interactions between HSCs/MPPs and niche cells

During embryogenesis, the FL provides a supportive niche for HSC/MPP development, however, the manner by which HSCs interact dynamically with their niche components remains elusive. To this end, we used CellPhoneDB[33,34] to construct an unbiased HSC/MPP-niche cell interaction network, with a focus on structural niche cells and macrophages (Fig. 3a), the latter of which have been shown to act as a niche component for HSC/MPP development in the FL equivalent of zebrafish[35] and mouse AGM region[36]. In-depth analysis identified several well-known ligand−receptor interactions involved in HSC/MPP development, such as TGFB1−TGFBR1, TEK−ANGPT1, and IGF2−IGF1R[37-39]. Importantly, we identified several previously unrecognized ligand−receptor interactions (Fig. 3b, c), including those related to cell growth (FLT1−VEGFB, HGF-CD44, MDK-LPR1, IGF1−IGF1R, and PTN−PTPRS)[40-43], cytokine (CCL3−IDE and CCL4−SLC7A1)[44], and Notch signaling (DLK1−NOTCH3 and DLK−NOTCH4)[45].

To determine whether the predicted signaling interactions indeed exist among the anatomically-organized cells, we performed 10x Visium ST using four slices from an E14.5

embryo along the dorsal-ventral axis, with a focus on the FL region (Fig. 3d-f). We also assessed the performance of ST using region specific markers, such as lung and intestine regions (Supplementary information, Fig. S5a). The joint dataset of FL region consisted of 3,791 individual spots after filtering (Supplementary information, Fig. S5b, c). To show the spatial organization of principal cell types in an unbiased manner, we performed deconvolution analysis[46,47] by assigning an enrichment score for each spot with cell type signature genes derived from scRNA-seq. After deconvolution, two spot patterns (first pattern and second pattern) were shown based on the enrichment score of top two cell types, and then mapped to the original FL region (Fig. 3g, h). As expected, erythroid cells and hepatoblasts showed the highest enrichment score in most spots, indicating that they are the predominated cell components of FL. To specifically determine the spatial organization of HSCs/MPPs and their interactive niche cells (ECs, stromal cells, hepatoblasts and macrophages), we regarded the spots as credible for one cell type, according to that the enrichment score of those cell types is higher than a threshold (80% to HSCs/MPPs and 70% to niche cells), and then mapped them to the original FL region (Supplementary information, Fig. S6a). To evaluate the performance of ST in resolving spatial organization, we examined the expression of cell type-specific genes in the candidate spots. As expected, *Hlf* and *Mecom* were selectively enriched in the HSC/MPP-localized spots (Supplementary information, Fig. S6b); *Ly86* and *Cd68* were specifically expressed in the macrophage-localized spots (Supplementary information, Fig. S6g); and the similar results were also observed in the structural niche cells-localized spots (Supplementary information, Fig. S6c-f). Taken together, ST profiles the spatial organization of FL for further decoding cell-cell interactions predicted by scRNA-seq (see below).

222

223 **Identification of expansion units of HSCs/MPPs**

224 To determine the architectural basis of cell-cell interactions, we defined HSC/MPP-localized
225 spots as intra-spots (indicating the closest relationship), HSC/MPP-surrounded spots as inter-
226 spots (indicating the second closest relationship), and other distant spots (indicating nearly no
227 interactive relationship) (Fig. 4a). For each niche cell type, analysis of enrichment score for
228 different types of spots showed that EC with the highest score for intra-spots was close to
229 HSCs/MPPs, which is consistent with a previous report[13]; hepatoblast and stromal cell with the
230 highest scores respectively for inter-spots and other distant spots were less close to HSCs/MPPs;
231 unexpectedly, macrophage with the higher score for intra- and inter-spots than that for other
232 distant spots was considered as a novel niche component spatially close to HSCs/MPPs (Fig.
233 4b). To quantitatively compare the interaction between HSCs/MPPs and different niche cells,
234 we defined an enrichment fold based on the ratio of the enrichment score median for each spot
235 type to the enrichment score median for all spots. Consequently, we found that macrophage
236 showed a 11.52-fold enrichment in the intra-spots and a 1.31-fold in the inter-spots, EC showed
237 a 1.62-fold enrichment in the intra-spots, while hepatoblast and stromal cell showed less
238 enrichment in the intra-spots (Fig. 4c, d; Supplementary information, Fig. S7a). Furthermore,
239 to validate the spatial relationship at nearly single-cell resolution, we analyzed the mouse E13.5
240 FL ST data based on Stereo-seq, which is a sequencing-based spatially resolved transcriptomic
241 technology with subcellular resolution[48]. We defined 20 bins as a spot (10-15 μm in diameter),
242 which may include 1-3 cell (s), and then annotated the spots (including intra-spots$^{Stereo\text{-}seq}$, inter-
243 spots$^{Stereo\text{-}seq}$ and other distant spots$^{Stereo\text{-}seq}$) referring to the aforementioned pipeline. As a result,

we found that macrophages showed a high enrichment both in intra-spots$^{Stereo\text{-}seq}$ and inter-spots$^{Stereo\text{-}seq}$ (Supplementary information, Fig. S7b). Finally, the consistent result was validated by CSOmap[49], an analytic method to reconstruct the cell spatial organization *de novo* based on scRNA-seq data (Supplementary information, Fig. S7c-f). Taken together, the results from three analytic methods of spatial information support that macrophage serve as an important niche cell with the closest relationship with HSCs/MPPs.

At molecular level, we examined the spatial expression of interactive signals predicted by CellPhoneDB analysis, and found that genes encoding ligands, such as MDK and PTN, were highly expressed in niche cells of intra-spots and inter-spots (Fig. 4e-i), and genes related to receptors, such as LRP1 and PTPRS, were enriched in HSCs/MPPs-localized spots (Fig. 4e-i). These results indicate that spatial proximity facilitates the signaling interactions for functionally supporting HSC/MPP expansion. Given that the intra-spots and inter-spots were characterized by spatially-proximal relationship among cells and enriched interactive signals, we defined them as expansion units, in which HSCs/MPPs located at the core of spots and interacted with surrounding niche cell spots (Fig. 4f, h, i). Taken together, we demonstrate that FL HSCs/MPPs expand in a number of units, in which macrophages and several growth factors, including MDK and PTN, are highly enriched.

Functional validation of role of niche cells in promoting HSC/MPP expansion

To determine how macrophages modulate HSC/MPP expansion in the FL, we firstly examined the spatial relationship between HSCs/MPPs and macrophages at E14.5. Immunofluorescence assay revealed two spatial patterns, one was that HSCs/MPPs attach proximal macrophages,

the other was that HSCs/MPPs are surrounded by macrophages (Fig. 5a-d). Of note, the latter pattern is similar to that between hematopoietic stem and progenitor cells and ECs in the FL equivalent of zebrafish[50], suggesting that macrophages may promote HSC/MPP expansion via forming a 'pocket-like' architecture. Functionally, E14.5 HSCs/MPPs were co-cultured with macrophages or cultured in the defined medium supplemented with macrophage-derived MDK. As expected, we found that HSC/MPP expansion was enhanced in macrophage co-cultured or MDK-supplemented systems, suggesting that macrophages can facilitate HSC/MPP expansion via secreting MDK factor (Fig. 5e-g). Furthermore, to determine whether the depletion of macrophages within FL niche will affect HSC/MPP expansion, macrophages were firstly depleted by using apoptosis-inducing clodronate-liposomes (Supplementary information, Fig. S8a-d)[36], and then we found that the absolute number of FL cells and the proportion of HSCs/MPPs (LSK cells and SLAM-LSK cells) were decreased at E14.5 (Fig. 5h-l).

Given that the FL is a transitory reservoir for both EMP- and HSC/MPP-derived macrophages[51], we thus performed bioinformatic analysis, immunofluorescence imaging and co-culture assay to determine which type of macrophages are in close contact to HSCs/MPPs. Firstly, by performing analyses of signature gene expression, developmental trajectory, and transcriptomic correlation, we found that macrophage1 (Mac1) and macrophage2 (Mac2) were derived from HSCs/MPPs and EMPs, respectively (Supplementary information, Fig. S9a-e). Then, we examined the spatial relationship between macrophages (Mac1 and Mac2) and HSCs/MPPs by 10x Visium ST. As a result, we found that both Mac1 and Mac2 exhibited a high enrichment in the intra- and inter-spots (Supplementary information, Fig. S10a), indicating that they are both in close contact to HSCs/MPPs. Moreover, immunofluorescence imaging

showed that both Mac1 (marked by Ccr2[52,53]) and Mac2 (marked by Iba1 and LXRα/β[52,54]) exhibited an adjacent relationship with HSCs/MPPs (marked by Runx1, c-Kit and CD150[13,31,55]) at E14.5 (Supplementary information, Fig. S10b-g). Finally, to examine the effect of Mac1 and Mac2 on the HSC/MPP expansion, we sorted F4/80^{low} macrophages (CD45^{+}CD11b^{+}F4/80^{low}[53,56], similar to Mac1), F4/80^{high} macrophages (CD45^{+}CD11b^{low}F4/80^{high}[53,56], similar to Mac2), and performed co-culture assay with mouse HSCs/MPPs (LSK) at E14.5, respectively. As a result, we found that HSC/MPP expansion was enhanced both in Mac1- and Mac2-co-cultured systems (Supplementary information, Fig. S10h). Taken together, these results suggest that both EMP- and HSC/MPP-derived macrophages play important roles in supporting HSC/MPP expansion.

In addition to macrophages, a meaningful proportion of HSC/MPP expansion units were also composed of three structural niche cells (Supplementary information, Fig. S7g-i). Among them, a closer spatial relationship between HSCs/MPPs and ECs was uncovered by 10x Visium ST (Fig. 4b-d, Supplementary information, Fig. S7a). To characterize EC-forming niche of HSCs/MPPs in detail, we detected their spatial relationship. Immunofluorescence assay revealed that HSCs/MPPs were surrounded by ECs (Fig. 6a, b), and most of the HSCs/MPPs were close to arterial portal vessels labeled with EphrinB2[13], with a few HSCs/MPPs residing around hepatic veins labeled with EphB4[57] at E14.5 (Fig. 6c, d). These results indicate that HSCs/MPPs show preferential spatial association adjacent to a putative portal vessel niche in the FL. To functionally determine whether the predicted interactive signals derived from structural niche cells can regulate HSC/MPP expansion, we performed HSC/MPP expansion assay at E14.5 in the defined medium supplemented with IGF1, IGF2, HGF, and PTN,

respectively. Given that the function of IGFs is regulated by their carrier proteins, IGFBPs[58,59], we also examined the role of IGFBP1/5/7, whose gene expression was enriched in hepatoblasts, stromal cells, and ECs, respectively (Fig. 6e). Consequently, the efficiency of supporting HSC/MPP expansion in IGFBP5- and PTN-supplemented culture systems was higher than that in IGF1-, IGF2-, HGF-, IGFBP1- and IGFBP7-supplemented culture systems (Fig. 6f-h). Taken together, functional analysis validates the potential cell-cell interactions and underlying molecular mechanisms supporting HSC/MPP expansion.

Cross-species analysis of FL hematopoiesis between mice and humans

To analyze the conservation and divergence of FL hematopoiesis between mice and humans, we compared our scRNA-seq data with a recently published scRNA-seq atlas of the human FL[15]. A total of 6,325 single cells from the human FL at 11 post-conception weeks (PCW) and 8,404 cells from the mouse FL at E14.5 were subjected to unsupervised UMAP analysis (Fig. 7a; Supplementary information, Fig. S11a). The integrative analysis showed that the FL cell types and HSC/MPP multilineage (erythrocyte/myelocyte/lymphocyte) differentiation routes were well mixed between these two species (Fig. 7b). Moreover, comparison of mouse and human FL cell types showed that most cell types were highly correlated (Supplementary information, Fig. S11b). Taken together, these data reveal conserved cell types and hematopoietic differentiation routes between mouse and human FL.

To compare the transcriptome features of FL HSCs/MPPs between mice and humans, we performed DEG analysis between HSCs/MPPs and other cell clusters for each species and identified 39 canonical HSC/MPP signature genes that are conserved in humans and mice

(Supplementary information, Fig. S11c). Moreover, we performed GO analysis of the DEGs between mouse and human HSCs/MPPs. The results showed that the GO terms related to "regulation of DNA damage response," "regulation of interleukin-6 biosynthetic process," and "regulation of telomerase activity" were enriched in human HSCs/MPPs (Fig. 7c), supporting the idea that human HSCs/MPPs are susceptible to DNA damage[60,61]. By contrast, the GO terms "positive regulation of inflammatory response," "cellular response to type I interferon," and "negative regulation of viral entry into host cells" were enriched in mouse HSCs/MPPs, supporting the notion that mouse HSCs/MPPs are responsive to inflammatory signals (Fig. 7d)[62]. Given the different living environments between mice and humans, mouse HSCs/MPPs may be more resistant to pathogen-derived inflammation, whereas human HSCs/MPPs are likely more susceptible to radiation-induced DNA damage. The presence of these divergent transcriptome features of HSCs/MPPs therefore indicates that despite overall similarity, there also exist species-specific mechanisms of the adaptive response to external stimuli.

To determine whether the mechanisms of HSC/MPP expansion in mice are conserved in humans, we also constructed an HSC/MPP−niche cell interaction network in the human FL using CellPhoneDB. We found that HSCs/MPPs displayed the stronger interactions with macrophages and ECs than other two niche cells (Fig. 7e), which was also validated by CSOmap analysis (Supplementary information, Fig. S11d, e). In addition, we found that the interactions related to cell growth, cell adhesion, cytokine, and Notch signaling identified in mice also existed in humans (Fig. 7f). Functionally, we performed immunofluorescence imaging and validated the cell-cell interaction between macrophages (marked by CD68) and HSCs/MPPs (marked by CD34) in human FL at 11 PCW (Fig. 7g-i); meanwhile, human cord

blood (CB) $CD34^+$ HSCs/MPPs were co-cultured with mouse macrophages. After four-day co-culture, we found that the number of co-cultured CB $CD34^+$ HSCs/MPPs was more than (1.7 folds) that of CB HSCs/MPPs without macrophage co-culture, supporting that macrophages play a conserved role in supporting human HSC/MPP expansion (Fig. 7j). Taken together, these data are consistent with a model whereby many mechanisms of FL HSC expansion are conserved between humans and mice, but there are also species-specific transcriptome signatures in HSCs/MPPs.

DISCUSSION

Using a high-throughput scRNA-seq and high-spatial-resolution ST framework, we generated an integrated spatiotemporal transcriptome atlas of FL in mice (Supplementary information, Fig. S12). scRNA-seq and functional analyses revealed that CD93 can be applied to purify a subset with enhanced stem cell properties from heterogeneous FL HSCs/MPPs. Given that CD93-marked type 1 HSC precursors in mouse AGM region do not show enhanced reconstitution ability than the counterparts after co-culture with stromal cell[63], we reason that hematopoietic cell heterogeneity characterized by CD93 may be cell-type- and developmental stage-dependent. Importantly, by integrating transcriptome, immunostaining, and functional analyses, we identified the 'pocket-like' units for HSC/MPP expansion, termed as HSC PLUS. Furthermore, although cross-species comparison of the FL cell atlas between mice and humans showed some divergent transcriptome signatures of HSCs/MPPs indicative of a species-specific mechanism of the adaptive response to external stimuli, the overall transcriptional similarity as well as conserved expansion mechanisms of HSCs/MPPs underscores the values of mouse

models to provide guidance for the expansion of functional human HSCs/MPPs *ex vivo*.

A profound understanding of cellular and molecular mechanisms underlying HSC/MPP expansion is essential for establishing protocols of HSC/MPP expansion *ex vivo*. Previous studies have suggested that FL niche cells can support HSC/MPP expansion via paracrine signaling. For instance, ECs can secrete SCF, ANGPTL2, and IGF2 for HSC expansion[13]; hepatoblasts support HSC/MPP expansion by secreting ANGPTL3, IGF2, SCF, and TPO[12,64]; and stromal cells produce ANGPTL2/3 and IGF2 for HSC/MPP expansion[39,65]. However, how these different types of cells interact with each other to form distinct functional tissues/organs remains unclear. By integrative analysis of spatiotemporal transcriptome atlas and functional experiments, we, for the first time, defined the HSC PLUS as the smallest functional units of FL. Within the HSC PLUS, macrophages and expansion-favoring factors MDK, PTN, and IGFBP5 are enriched. Although the close spatial relationships between macrophages/ECs and HSCs/MPPs was also revealed by CSOmap analysis in human FL, further functional validation of the conserved mechanisms is warranted in future investigations. Taken together, our resource deepens the understanding of the crosstalk between HSCs/MPPs and niche cells, and provides novel insights into the generation of HSC PLUS-based culture system for HSCs/MPPs *ex vivo*.

Macrophages play an important role in immune defense, however, extensive studies have demonstrated their multiple functional roles beyond immune defense. For example, macrophages repair the ruptured brain vessels in zebrafish via adhesion and mechanical traction [66]; in mouse aorta, macrophages secret matrix metalloproteinase 9 to control the collagen production and prevent arterial stiffness[67]. Our immunofluorescence, integrative transcriptomics, and functional analyses identify an uncharacterized role of FL-resident

macrophages in facilitating HSC/MPP expansion. Interestingly, macrophages form a 'pocket-like' architecture surrounding inside HSCs/MPPs, which is architecturally similar to EC 'pocket' observed in E11.5 mouse FL[50]. Of note, the existence of 'pocket-like' architecture formed by different niche cells may be partially explained by that a specialized microenvironment could effectively enhance cell-cell interaction by increasing the concentration of local signaling molecules[50], such as Ccl21 from ECs[55] and MDK from macrophages (in this study). Taken together, our unbiased characterization of HSC/MPP niche components updates the paradigm that HSCs/MPPs preferentially reside in the perivascular niche and are regulated by ECs, hepatoblasts, and stromal cells[10-13,50].

In summary, our findings characterize HSC/MPP heterogeneity, expansion-favoring factors and architectural basis, and conserved expansion mechanisms in both mice and humans, which provides a valuable resource for studying HSC/MPP expansion. Further analysis of this resource will help to elucidate the mechanism underlying hematological malignancies of fetal origin.

MATERIALS AND METHODS

Experimental model

Mouse lines

Wild-type C57BL/6 mice were purchased from SPF (Beijing) Biotechnology Co., Ltd. CD93 genetic mutant mice were generated as previously described[68]. B6.SJL (CD45.1) mice were purchased from the Institute of Laboratory Animal Science (ILAS), Chinese Academy of Medical Sciences (CAMS). All mice were bred under specific pathogen-free conditions (animal license number: SYXK (Beijing) 2018-0021). For transplantation assays, male CD45.1 mice were crossed with female CD45.2 mice to obtain CD45.1/.2 embryos; the morning that the vaginal plug was detected was defined as embryonic day (E) 0. The present study was approved by the Ethical Review Committee of the Institute of Zoology, Chinese Academy of Sciences, China.

Human samples

Human embryos were obtained following electively terminated pregnancies at Haidian Maternal & Child Health Hospital in Beijing. All experiments were performed in accordance with protocols approved by the Peking University Institutional Review Board (PUIRB) (certificate number: IRB00001052-18083)[69] and the Ethics Committee of the Institute of Zoology, Chinese Academy of Sciences. Written informed consent was obtained before sample collection.

Human cord blood (CB) samples were collected from healthy volunteers after informed consents obtained. All experiments were performed in accordance with protocols approved by the Research Ethics Committee of Beijing Institute of Transfusion Medicine and the Ethics Committee of the Institute of Zoology, Chinese Academy of Sciences. $CD34^+$ HSCs/MPPs from human CB were performed in accordance with protocols[70,71].

Flow cytometry

Single-cell suspensions from the FL were prepared by mechanical dissociation, and the cells were stained for 30 min at 4℃. Antibodies used in this study included those against: Lineage-FITC (Biolegend, 133302), 7-AAD (Biolegend, 420404), CD117-APC (eBioscience, 17-1171-82), CD117-PE-Cyanine5 (eBioscience, 15-1171-81), CD117- APC-eFluor 780 (eBioscience, 47-1171-82), Ly-6A/E-PE-Cyanine7 (eBioscience, 25-5981-81), CD135-PE-Cyanine5 (eBioscience, 15-1351-82), CD135-APC (Biolegend, 135309), CD45.1-FITC (eBioscience, 11-0451-81), CD45.2-PE-Cyanine7 (eBioscience, 25-0454-80), CD3e-APC (eBioscience, 17-0031-81), B220-PE (eBioscience, 12-0452-81), CD11b-APC (eBioscience, 17-0112-81), Ly6G/Ly-6C-PE (eBioscience, 12-5931-81), CD150-PE (eBioscience, 12-1502-82), CD48-APC-eFluor780 (eBioscience, 47-0481-82), CD93-APC (eBioscience, 17-5892-81), CD45-FITC (eBioscience, 11-0451-82), CD68- PE-Cyanine7 (eBioscience, 25-0681-80), CD34-APC (BD, 560940) and APC-Cyanine7-F4/80 (Biolegend, 123117). 7-AAD viability staining solution was used to exclude dead cells. Flow cytometry was performed using MoFlo XDP (Beckman Coulter) and the analysis was carried out with Flowjo (vX.7.0).

HSC/MPP cell culture

100 HSCs/MPPs from E14.5 FL, including $Lin^{-}Sca\text{-}1^{+}c\text{-}Kit^{+}$ (LSK), $Flit3^{-}LSK$, $CD150^{+}CD48^{-}$ LSK (SLAM-LSK), were alone cultured in 100 μL StemSpan medium in a well of 96 U-well plate for 15 days. The culture medium was supplemented with 50 ng/mL SCF (Peprotech), 30 ng/mL FLT3L (Peprotech), 20 ng/mL TPO (Peprotech), and 10 ng/mL IL-6 (Peprotech). The expansion medium was supplemented with 50 ng/mL IGF1, IGF2, IGFBP1, IGFBP5, IGFBP7, PTN, MDK, respectively.

E14.5 HSCs/MPPs (LSK cells) at a density of 2×10^3 cells were co-cultured with 2×10^4 $F4/80^{low}$ macrophages ($CD45^+CD11b^+F4/80^{low}$), $F4/80^{high}$ macrophages ($CD45^+CD11b^{low}F4/80^{high}$) or macrophages (containing half of $F4/80^{low}$ and half of $F4/80^{high}$ macrophages) in 500 μL MyeloCult M5300 medium in a well of 24-well plate for 4 days. The culture medium was supplemented with 50 ng/mL SCF (Peprotech), 30 ng/mL FLT3L (Peprotech), 20 ng/mL TPO (Peprotech), and 10 ng/mL IL-6 (Peprotech).

Human CB $CD34^+$ HSCs/MPPs at a density of 2×10^3 cells were co-cultured with 2×10^4 mouse macrophages in 500 μL StemSpan medium in a well of 24-well plate for 4 days. The culture medium was supplemented with 50 ng/mL Recombinant Human SCF (Peprotech), 50 ng/mL FLT3L (Peprotech), 50 ng/mL TPO (Peprotech).

Clodronate-liposome treatment

For the clodronate-liposome treatment, pregnant females were injected with Clodronate-liposome and Control-liposome (CP-005-005, LIPOSOME) as dose of 1mg $20g^{-1}$ mouse body weight at E11.5, E12.5 and E13.5, respectively, and the macrophage depletion and FL HSC/MPP phenotype were measured at E14.5.

Immunofluorescence

Immunofluorescence assay for embryos was performed as previously described[72]. The E14.5 embryos or human FL (11 PCW) were fixed in 4% paraformaldehyde/PBS overnight at 4°C. After gradient dehydration in 15% and 30% sucrose/PBS at 4°C, these embryos were embedded and frozen in OCT overnight at -80°C. The following day, embryos were sectioned to 10-μm-thick slides and blocked for 2 h at room temperature with 5% BSA/PBS containing 0.3% Triton X-100. After washing three times in PBS, 15 min/time on an orbital shaker, the slides were

incubated overnight at 4°C with primary antibodies diluted in 1% BSA/PBS. The following day, the slices were washed three times in PBS containing 0.1% Tween-20, 15 min/time on an orbital shaker, and incubated for 2 h at room temperature with secondary antibodies diluted in 1% BSA/PBS. Nuclei were stained with Hoechst 33342 (Invitrogen) and immunofluorescence images were obtained using a laser scanning confocal microscope (A1; Nikon). The primary antibodies used in the assays included those against: Runx1 (1:800; abcam), CD150 (1:200, BD), CD150 (1:200, Biolegend), c-Kit (1:300; BD), c-Kit (1:200; Biolegend), Hlf (1:100, ABclonal), Mecom (1:200, ABclonal), EphrinB2 (1:300; R&D), Ephb4 (1:300; R&D), Lyve1 (1:800; R&D), F4/80 (1:800, Santa Cruz), LXRα/β (1:500, Santa Cruz), Iba1 (1:500, Santa Cruz), Ccr2 (1:250; abcam), human anti-CD34 antibody (1:250; abcam), human anti-CD68 antibody (1:200; Biolegend). The secondary antibodies used in the assays included goat anti-rabbit IgG Alexa Fluor 488 (1:800; Life Technologies), goat anti-rabbit IgG Alexa Fluor 594 (1:800; Life Technologies), donkey anti-rat IgG Alexa Fluor 488 (1:800; Life Technologies), goat anti-rat IgG Alexa Fluor 594 (1:800; Life Technologies), goat anti-mouse IgG Alexa Fluor 488 (1:800; Life Technologies), goat anti-mouse IgG Alexa Fluor 555 (1:800; Life Technologies) and donkey anti-goat IgG Alexa Fluor 647 (1:300; Life Technologies),

Colony-forming unit (CFU) culture assay

Single-cell suspensions of sorted E14.5 HSCs/MPPs in combination of CD93 and other HSC/MPP markers were cultured in M3434 medium (Stem Cell Technologies, 03434) at 37°C with 5% CO_2 for 10 days. Subsequently, the number of each type of colony, including CFU-E, CFU-GM, and CFU-GEMM, was counted based on morphology. More than three groups of independent experiments were analyzed. CFU-E, CFU-erythroid; CFU-GEMM, CFU-

granulocyte, erythroid, macrophage, megakaryocyte; CFU-GM, CFU-granulocyte, macrophage.

Transplantation assay

CD45.2 recipients received a split lethal dose (9 Gy) of X-ray irradiation (RS2000). For the primary transplantation assay, a total of 500 $CD93^{+}$HSCs/$CD93^{-}$HSCs or 2,000 LSK/$CD93^{+}$LSK cells were sorted from E14.5 FL along with 4×10^4 CD45.2 nucleated bone marrow (BM) cells and intravenously injected into the tail vein of the recipients. For the secondary transplantation assay, 1×10^6 BM cells from donor mice were mixed with 4×10^4 CD45.2 nucleated BM cells and intravenously injected into the tail vein of the recipients. The chimerism and the multi-lineage reconstitution ability were analyzed using peripheral blood (PB) from the recipients.

Western blotting

Western blotting was performed as previously described[72]. The protein extracted from E14.5 fetal liver cells with cell lysis buffer (10 mM Tris-HCl, pH 8.0, 10 mM NaCl, and 0.5% NP-40) containing protease inhibitor (no.04693116001; Roche). The protein level of CD93 was detected using the following antibodies: anti-β actin (1:2,000, Cell Signaling Technology). Anti-CD93 (1:1,000, abcam).

Cell preparation for single-cell RNA-sequencing (scRNA-seq)

Fluorescence-activated cell sorting was performed at four time points to separately sort hematopoietic cells (HCs), endothelial cells (ECs), and non-hematopoietic/non-endothelial cells (NCs) from the FL, and subsequently pooled them together for sequencing. At E11.5, $CD45^{+}$HCs[9,73] and $CD45^{-}$ non-HCs were pooled together for sequencing. At E12.5, E13.5, and

E14.5, LSK cells[74,75], $CD45^+$HCs, $CD45^-CD31^+$ECs[76], and $CD45^-CD31^-$ NCs were pooled together for sequencing.

Processing of scRNA-seq data

To capture individual cells, we utilized the Chromium Single Cell 2' Reagent Version 1 Kit (10x Genomics). The quality of the sequencing reads was evaluated by FastQC and MultiQC. Cell Ranger v2.2.0 was used to align the sequencing reads to the mm10 mouse reference genome and quantitate the expression of transcripts in each cell. R v3.6.0 and the package Seurat v3.1.2 were used for the downstream analyses. Cells with fewer than 250 detected genes, less than 500 unique molecular identifiers (UMIs), or more than 10% mitochondrial UMIs were removed. Finally, we detected an average of 3,503 genes per cell.

Batch correction and dimension reduction

To minimize technical variability due to sample collection time points while preserving biological variation, two functions in Seurat, FindIntegrationAnchors and IntegrateData, were used for batch correction among cells at the four embryonic stages. Specifically, only principal components analysis (PCA) and PCA-dependent analyses were performed using batch-corrected data.

Dimension reduction includes three stages of analysis: selection of variable genes (FindVariableGene), PCA (RunPCA, from variable genes), and uniform manifold approximation and projection (UMAP). After quantity control, we obtained 32,449 high-quality single cells for further analysis. Subsequently, we performed PCA using the 2,000 most variable genes selected by the FindIntegrationAnchors function. The top 30 principal components (PCs) were selected for UMAP to obtain bidimensional coordinates for each cell.

To dissect the potential relationship among HSCs/MPPs, progenitors, and macrophages, we also performed PHATE analysis using the same 2,000 genes.

Unsupervised clustering and annotation

We performed the FindNeighbors and FindClusters functions (resolution = 0.5) to cluster cells using the Louvain algorithm based on the top 30 PCs. The final number of cell clusters was found to be 21 by selecting a resolution of 0.5. The known markers used for cell cluster annotation are listed in **Table S1**.

Identification of differentially expressed genes

We used the FindAllMarkers function (logfc. threshold = log(1.2)) based on normalized data to identify differentially expressed genes (DEGs). *P*-value adjustment was performed using Bonferroni correction based on the total number of genes in the dataset. DEGs with adjusted *P*-values > 0.05 were filtered out. GO analyses were performed using the R package cluster profiler[77].

Cell-cell interaction analysis

CellPhoneDB[33,34] was used to infer enriched ligand−receptor interactions based on the gene expression of a ligand in one cell type and its receptor in another cell type. Selected ligand−receptor pairs enriched between HSCs and niche cells or macrophages were visualized. We only considered the ligands expressed in more than 20%, and receptors expressed in more than 4%, of cells in one cluster.

10x Visium Spatial Transcriptomics (ST)

Staining and imaging

E14.5 embryos were embedded in tissue-Tek (OCT) and snap-frozen using dry ice slurry.

Cryosections were cut at 10-μm thickness, mounted onto the GEX arrays. Sections were placed on Thermocycler Adaptor with the active surface facing up and incubate 1 min at 37°C, and fixed for 30 min with methyl alcohol in -20°C, followed by staining with H&E (Eosin, Dako CS701, Hematoxylin Dako S3309, bluing buffer CS702). The brightfield images were taken on a Leica DMI8 whole-slide scanner at 10x resolution.

Permeabilization and reverse transcription

Visum spatial gene expression was processed using Visum spatial gene expression slide and Reagent Kit (10x Genomics, PN-1000184). For each well, Slide Cassette was used to create leakproof wells for adding reagents. 70 μL Permeabilization enzyme were added and incubated at 37°C for 20 min. Each well was washed with 100 μL SSC, and 75 μL reverse transcription Master Mix was added for cDNA Synthesis.

cDNA library preparation for sequencing

At the end of first-strand synthesis, remove RT Master Mix from the wells. Add 75 μL 0.08 M KOH and incubate 5 min at room temperature, then remove the KOH from wells and washed with 100 μL EB buffer. Add 75 μL Second Strand Mix to each well for second-strand synthesis. cDNA amplification was performed on a S1000TM Touch Thermal Cycler (Bio Rad). According to the manufacture's introduction, Visum spatial libraries were constructed using Visum spatial Library construction kit (10x Genomics, PN-1000184). The libraries were finally sequenced using an Illumina Novaseq6000 sequencer with a sequencing depth of at least 100,000 reads per spot with pair-end 150 bp (PE150) reading strategy (performed by CapitalBio Technology, Beijing).

Processing of the spatial transcriptomics data

To annotate spots, we applied the integration workflow introduced in Seurat v3, which enables the probabilistic transfer of cell types from the scRNA-seq data to the ST data. Specifically, we first identified pairwise correspondences between single cells and single spots to quantify the batch effect. Each spot was then annotated based on the transcriptomic similarity between spots and cell types in the scRNA-seq dataset. This probabilistic transfer procedure was implemented using the FindTransferAnchors (dims = 1:30) and TransferData (dims = 1:30) functions in Seurat with the combination of top 100 DEGs of each cell type.

Cross-species analysis of FL in between mouse and human

We obtained single-cell transcriptome data of human FL from ArrayExpress under the accession code E-MTAB-7407. Firstly, we analyzed gene expression matrices of 6,325 human FL cells at 11 post-conception weeks and 8,404 mouse FL cells at E14.5 after filtering low-quality cells. We then filtered mouse−human ortholog genes based on the Mouse Genome Informatics (MGI) database (http://www.informatics. jax.org/downloads/reports/HMD_HumanPhenotype.rpt), and obtained 13,819 homologous genes with a one-to-one translation between humans and mice for further analysis. Next, the merge function was used to combine human and mouse FL cells, and further analysis was performed including UMAP, differential expression, and Pearson correlation using the same methods described above.

Quantitation and statistical analysis

GraphPad Prism 6 was used to analyze the data. Values are presented as the mean ± SEM. A Student's unpaired two-tailed t-test was applied for comparisons unless otherwise indicated.

DATA AVAILABILITY

The scRNA-seq and 10x Visium ST datasets generated in the present study are available at https://bigd.big.ac.cn/gsub/ in BIG Submission Portal, under the accession number CRA002489 and CRA003651, respectively. The E13.5 Stereo-seq dataset used in the present study is kindly provided by Prof. Xun Xu and Prof. Longqi, Liu.

ACKNOWLEDGMENTS

We thank Yiwei Lai (BGI-ShenZhen, Shenzhen, China) for data transmission of E13.5 Stereo-seq dataset. This work was supported by grants from the National Key Research and Development Program of China (2018YFA0800200, 2018YFA0801000, 2016YFA0100500 to F.L., and 2016YFA0100103 to C.L.), the Strategic Priority Research Program of the Chinese Academy of Sciences, China (XDA16010207 to F.L.), the National Natural Science Foundation of China (31830061, 81530004, 31425016 to F.L., and 31871266 to C.L.), and NSFC Key Research Grant 71532001 (to C.L.). Part of the data analysis was performed on the High-Performance Computing Platform of the Center for Life Sciences, Peking University.

AUTHORSHIP CONTRIBUTIONS

S.G. and F.L. conceived the project, analyzed the data, and wrote the paper; S.G. performed most of the experiments with help from Y.Z., G.L., B.H., D.M., and L.W.; Q.S. and Z.K. performed the bioinformatics analysis under the guidance of C.L.; J.J. provided CD93 genetic mutant mice; X.F. provided human CB sample; C.X. provided human FL sample; X.X. and L.L. provided E13.5 FL Stereo-seq dataset; B.G. interpreted the data and assisted with the manuscript. All authors read and approved the final manuscript.

CONFLICT OF INTEREST DISCLOSURES

The authors declare no competing interests.

REFERENCES

1 Yamamoto, R. *et al.* Clonal analysis unveils self-renewing lineage-restricted progenitors generated directly from hematopoietic stem cells. *Cell* **154**, 1112-1126, doi:10.1016/j.cell.2013.08.007 (2013).

2 Wilkinson, A. C., Igarashi, K. J. & Nakauchi, H. Haematopoietic stem cell self-renewal in vivo and ex vivo. *Nat Rev Genet* **21**, 541-554, doi:10.1038/s41576-020-0241-0 (2020).

3 Calvanese, V. *et al.* MLLT3 governs human haematopoietic stem-cell self-renewal and engraftment. *Nature* **576**, 281-286, doi:10.1038/s41586-019-1790-2 (2019).

4 Wilkinson, A. C. *et al.* Long-term ex vivo haematopoietic-stem-cell expansion allows nonconditioned transplantation (vol 571, pg 117, 2019). *Nature* **571**, doi:10.1038/s41586-019-1395-9 (2019).

5 McGrath, K. E., Frame, J. M. & Palis, J. Early hematopoiesis and macrophage development. *Semin Immunol* **27**, 379-387, doi:10.1016/j.smim.2016.03.013 (2015).

6 Hoeffel, G. & Ginhoux, F. Ontogeny of Tissue-Resident Macrophages. *Front Immunol* **6**, 486, doi:10.3389/fimmu.2015.00486 (2015).

7 Ema, H. & Nakauchi, H. Expansion of hematopoietic stem cells in the developing liver of a mouse embryo. *Blood* **95**, 2284-2288, doi:DOI 10.1182/blood.V95.7.2284.007k14_2284_2288 (2000).

8 Mikkola, H. K. A. & Orkin, S. H. The journey of developing hematopoietic stem cells. *Development* **133**, 3733-3744, doi:10.1242/dev.02568 (2006).

9 Rybtsov, S., Ivanovs, A., Zhao, S. L. & Medvinsky, A. Concealed expansion of immature precursors underpins acute burst of adult HSC activity in foetal liver. *Development* **143**, 1284-1289, doi:10.1242/dev.131193 (2016).

10 Lee, Y., Leslie, J., Yang, Y. & Ding, L. Hepatic stellate and endothelial cells maintain hematopoietic stem cells in the developing liver. *J Exp Med* **218**, doi:10.1084/jem.20200882 (2021).

11 Swain, A., Inoue, T., Tan, K. S., Nakanishi, Y. & Sugiyama, D. Intrinsic and extrinsic regulation of mammalian hematopoiesis in the fetal liver. *Histol Histopathol* **29**, 1077-1082, doi:10.14670/HH-29.1077 (2014).

12 Schmelzer, E. Hepatic progenitors of the fetal liver: Interactions with hematopoietic stem cells. *Differentiation* **106**, 9-14, doi:10.1016/j.diff.2019.02.005 (2019).

13 Khan, J. A. *et al.* Fetal liver hematopoietic stem cell niches associate with portal vessels. *Science* **351**, 176-180, doi:10.1126/science.aad0084 (2016).

14 Han, X. *et al.* Mapping the Mouse Cell Atlas by Microwell-Seq. *Cell* **172**, 1091-1107 e1017, doi:10.1016/j.cell.2018.02.001 (2018).

15 Popescu, D. M. *et al.* Decoding human fetal liver haematopoiesis. *Nature* **574**, 365-371, doi:10.1038/s41586-019-1652-y (2019).

16 Stahl, P. L. *et al.* Visualization and analysis of gene expression in tissue sections by spatial transcriptomics. *Science* **353**, 78-82, doi:10.1126/science.aaf2403 (2016).

17 McKinney-Freeman, S. *et al.* The transcriptional landscape of hematopoietic

stem cell ontogeny. *Cell Stem Cell* **11**, 701-714, doi:10.1016/j.stem.2012.07.018 (2012).

18 Gao, S. & Liu, F. Fetal liver: an ideal niche for hematopoietic stem cell expansion. *Sci China Life Sci* **61**, 885-892, doi:10.1007/s11427-018-9313-4 (2018).

19 Becht, E. *et al.* Dimensionality reduction for visualizing single-cell data using UMAP. *Nat Biotechnol* **37**, 38-+, doi:10.1038/nbt.4314 (2019).

20 Zhang, Y. *et al.* PR-domain-containing Mds1-Evi1 is critical for long-term hematopoietic stem cell function. *Blood* **118**, 3853-3861, doi:10.1182/blood-2011-02-334680 (2011).

21 Yokomizo, T. *et al.* Hlf marks the developmental pathway for hematopoietic stem cells but not for erythro-myeloid progenitors. *J Exp Med* **216**, 1599-1614, doi:10.1084/jem.20181399 (2019).

22 Huang, K. L. *et al.* A common haplotype lowers PU.1 expression in myeloid cells and delays onset of Alzheimer's disease. *Nat Neurosci* **20**, 1052-1061, doi:10.1038/nn.4587 (2017).

23 Tober, J. *et al.* Maturation of hematopoietic stem cells from prehematopoietic stem cells is accompanied by up-regulation of PD-L1. *J Exp Med* **215**, 645-659, doi:10.1084/jem.20161594 (2018).

24 Hamey, F. K. & Gottgens, B. Machine learning predicts putative hematopoietic stem cells within large single-cell transcriptomics data sets. *Exp Hematol* **78**, 11-20, doi:10.1016/j.exphem.2019.08.009 (2019).

25 Moon, K. R. *et al.* Visualizing structure and transitions in high-dimensional biological data. *Nat Biotechnol* **37**, 1482-1492, doi:10.1038/s41587-019-0336-3 (2019).

26 Jordan, C. T., McKearn, J. P. & Lemischka, I. R. Cellular and developmental properties of fetal hematopoietic stem cells. *Cell* **61**, 953-963, doi:10.1016/0092-8674(90)90061-i (1990).

27 Rebel, V. I. *et al.* A comparison of long-term repopulating hematopoietic stem cells in fetal liver and adult bone marrow from the mouse. *Exp Hematol* **24**, 638-648 (1996).

28 Harrison, D. E., Zhong, R. K., Jordan, C. T., Lemischka, I. R. & Astle, C. M. Relative to adult marrow, fetal liver repopulates nearly five times more effectively long-term than short-term. *Exp Hematol* **25**, 293-297 (1997).

29 Zeigler, F. C., Bennett, B., Jordan, C. T., Bauer, K. & Matthews, W. Cellular and Molecular Characterization of the Role of the Flk-2 Flt-3 Receptor Tyrosine Kinase in Hematopoietic Stem-Cells. *Blood* **84**, A415-A415 (1994).

30 Kim, I., He, S. H., Yilmaz, O. H., Kiel, M. J. & Morrison, S. J. Enhanced purification of fetal liver hematopoietic stem cells using SLAM family receptors. *Blood* **108**, 737-744, doi:10.1182/blood-2005-10-4135 (2006).

31 Toyama, H., Arai, F., Hosokawa, K., Ikushima, Y. M. & Suda, T. N-cadherin+ HSCs in fetal liver exhibit higher long-term bone marrow reconstitution activity than N-cadherin- HSCs. *Biochem Biophys Res Commun* **428**, 354-359, doi:10.1016/j.bbrc.2012.10.058 (2012).

32 Iwasaki, H., Arai, F., Kubota, Y., Dahl, M. & Suda, T. Endothelial protein C receptor-expressing hematopoietic stem cells reside in the perisinusoidal niche in fetal liver. *Blood* **116**, 544-553, doi:10.1182/blood-2009-08-240903 (2010).

33 Vento-Tormo, R. *et al.* Single-cell reconstruction of the early maternal-fetal interface in humans. *Nature* **563**, 347-353, doi:10.1038/s41586-018-0698-6 (2018).

34 Efremova, M., Vento-Tormo, M., Teichmann, S. A. & Vento-Tormo, R. CellPhoneDB: inferring cell-cell communication from combined expression of multi-subunit ligand-receptor complexes. *Nat Protoc* **15**, 1484-1506, doi:10.1038/s41596-020-0292-x (2020).

35 Li, D. *et al.* VCAM-1(+) macrophages guide the homing of HSPCs to a vascular niche. *Nature* **564**, 119-124, doi:10.1038/s41586-018-0709-7 (2018).

36 Mariani, S. A. *et al.* Pro-inflammatory Aorta-Associated Macrophages Are Involved in Embryonic Development of Hematopoietic Stem Cells. *Immunity* **50**, 1439-1452 e1435, doi:10.1016/j.immuni.2019.05.003 (2019).

37 Vaidya, A. & Kale, V. P. TGF-beta signaling and its role in the regulation of hematopoietic stem cells. *Syst Synth Biol* **9**, 1-10, doi:10.1007/s11693-015-9161-2 (2015).

38 Ikushima, Y. M. *et al.* Enhanced Angpt1/Tie2 signaling affects the differentiation and long-term repopulation ability of hematopoietic stem cells. *Biochem Biophys Res Commun* **430**, 20-25, doi:10.1016/j.bbrc.2012.11.002 (2013).

39 Zhang, C. C. & Lodish, H. F. Insulin-like growth factor 2 expressed in a novel fetal liver cell population is a growth factor for hematopoietic stem cells. *Blood* **103**, 2513-2521, doi:DOI 10.1182/blood-2003-08-2955 (2004).

40 Wong, J. C. *et al.* A glucocorticoid- and diet-responsive pathway toggles adipocyte precursor cell activity in vivo. *Sci Signal* **9**, ra103, doi:10.1126/scisignal.aag0487 (2016).

41 Caselli, A. *et al.* IGF-1-mediated osteoblastic niche expansion enhances long-term hematopoietic stem cell engraftment after murine bone marrow transplantation. *Stem Cells* **31**, 2193-2204, doi:10.1002/stem.1463 (2013).

42 Gealekman, O. *et al.* Enhanced angiogenesis in obesity and in response to PPARgamma activators through adipocyte VEGF and ANGPTL4 production. *Am J Physiol Endocrinol Metab* **295**, E1056-1064, doi:10.1152/ajpendo.90345.2008 (2008).

43 Imai, A. *et al.* Adrenomedullin Suppresses Vascular Endothelial Growth Factor-Induced Vascular Hyperpermeability and Inflammation in Retinopathy. *Am J Pathol* **187**, 999-1015, doi:10.1016/j.ajpath.2017.01.014 (2017).

44 Broxmeyer, H. E., Capitano, M., Campbell, T. B., Hangoc, G. & Cooper, S. Modulation of Hematopoietic Chemokine Effects In Vitro and In Vivo by DPP-4/CD26. *Stem Cells Dev* **25**, 575-585, doi:10.1089/scd.2016.0026 (2016).

45 Macedo, D. B. & Kaiser, U. B. DLK1, Notch Signaling and the Timing of Puberty. *Semin Reprod Med* **37**, 174-181, doi:10.1055/s-0039-3400963 (2019).

46 Fawkner-Corbett, D. *et al.* Spatiotemporal analysis of human intestinal development at single-cell resolution. *Cell* **184**, 810-826 e823, doi:10.1016/j.cell.2020.12.016 (2021).
47 Asp, M. *et al.* A Spatiotemporal Organ-Wide Gene Expression and Cell Atlas of the Developing Human Heart. *Cell* **179**, 1647-1660 e1619, doi:10.1016/j.cell.2019.11.025 (2019).
48 Chen, A. *et al.* Large field of view-spatially resolved transcriptomics at nanoscale resolution. *bioRxiv* (2021).
49 Ren, X. *et al.* Reconstruction of cell spatial organization from single-cell RNA sequencing data based on ligand-receptor mediated self-assembly. *Cell Res* **30**, 763-778, doi:10.1038/s41422-020-0353-2 (2020).
50 Tamplin, O. J. *et al.* Hematopoietic stem cell arrival triggers dynamic remodeling of the perivascular niche. *Cell* **160**, 241-252, doi:10.1016/j.cell.2014.12.032 (2015).
51 Varol, C., Mildner, A. & Jung, S. Macrophages: development and tissue specialization. *Annu Rev Immunol* **33**, 643-675, doi:10.1146/annurev-immunol-032414-112220 (2015).
52 Yahara, Y. *et al.* Erythromyeloid progenitors give rise to a population of osteoclasts that contribute to bone homeostasis and repair. *Nat Cell Biol* **22**, 49-59, doi:10.1038/s41556-019-0437-8 (2020).
53 Hoeffel, G. *et al.* C-Myb(+) erythro-myeloid progenitor-derived fetal monocytes give rise to adult tissue-resident macrophages. *Immunity* **42**, 665-678, doi:10.1016/j.immuni.2015.03.011 (2015).
54 Mass, E. *et al.* Specification of tissue-resident macrophages during organogenesis. *Science* **353**, doi:10.1126/science.aaf4238 (2016).
55 Xue, Y. Y. *et al.* The Vascular Niche Regulates Hematopoietic Stem and Progenitor Cell Lodgment and Expansion via klf6a-ccl25b. *Dev Cell* **42**, 349-+, doi:10.1016/j.devcel.2017.07.012 (2017).
56 Gomez Perdiguero, E. *et al.* Tissue-resident macrophages originate from yolk-sac-derived erythro-myeloid progenitors. *Nature* **518**, 547-551, doi:10.1038/nature13989 (2015).
57 Ozgur, E., Heidenreich, A., Dagtekin, O., Engelmann, U. & Bloch, W. Distribution of EphB4 and EphrinB2 in normal and malignant urogenital tissue. *Urol Oncol* **29**, 78-84, doi:10.1016/j.urolonc.2008.12.020 (2011).
58 Allard, J. B. & Duan, C. IGF-Binding Proteins: Why Do They Exist and Why Are There So Many? *Front Endocrinol (Lausanne)* **9**, 117, doi:10.3389/fendo.2018.00117 (2018).
59 Bach, L. A. IGF-binding proteins. *J Mol Endocrinol* **61**, T11-T28, doi:10.1530/JME-17-0254 (2018).
60 Doulatov, S., Notta, F., Laurenti, E. & Dick, J. E. Hematopoiesis: a human perspective. *Cell Stem Cell* **10**, 120-136, doi:10.1016/j.stem.2012.01.006 (2012).
61 Milyavsky, M. *et al.* A distinctive DNA damage response in human hematopoietic stem cells reveals an apoptosis-independent role for p53 in self-renewal.

Cell Stem Cell **7**, 186-197, doi:10.1016/j.stem.2010.05.016 (2010).

62 Mohrin, M. *et al.* Hematopoietic stem cell quiescence promotes error-prone DNA repair and mutagenesis. *Cell Stem Cell* **7**, 174-185, doi:10.1016/j.stem.2010.06.014 (2010).

63 Zhou, F. *et al.* Tracing haematopoietic stem cell formation at single-cell resolution. *Nature* **533**, 487-492, doi:10.1038/nature17997 (2016).

64 Chou, S. & Lodish, H. F. Fetal liver hepatic progenitors are supportive stromal cells for hematopoietic stem cells. *P Natl Acad Sci USA* **107**, 7799-7804, doi:10.1073/pnas.1003586107 (2010).

65 Zhang, C. C. *et al.* Angiopoietin-like proteins stimulate ex vivo expansion of hematopoietic stem cells. *Nat Med* **12**, 240-245, doi:10.1038/nm1342 (2006).

66 Liu, C. *et al.* Macrophages Mediate the Repair of Brain Vascular Rupture through Direct Physical Adhesion and Mechanical Traction. *Immunity* **44**, 1162-1176, doi:10.1016/j.immuni.2016.03.008 (2016).

67 Lim, H. Y. *et al.* Hyaluronan Receptor LYVE-1-Expressing Macrophages Maintain Arterial Tone through Hyaluronan-Mediated Regulation of Smooth Muscle Cell Collagen. *Immunity* **49**, 326-341 e327, doi:10.1016/j.immuni.2018.06.008 (2018).

68 Liang, Q., Su, L., Zhang, D. & Jiao, J. CD93 negatively regulates astrogenesis in response to MMRN2 through the transcriptional repressor ZFP503 in the developing brain. *Proc Natl Acad Sci U S A* **117**, 9413-9422, doi:10.1073/pnas.1922713117 (2020).

69 Wang, X. *et al.* Comparative analysis of cell lineage differentiation during hepatogenesis in humans and mice at the single-cell transcriptome level. *Cell Res* **30**, 1109-1126, doi:10.1038/s41422-020-0378-6 (2020).

70 Ding, N. *et al.* Global transcriptome analysis for identification of interactions between coding and noncoding RNAs during human erythroid differentiation. *Front Med* **10**, 297-310, doi:10.1007/s11684-016-0452-0 (2016).

71 Ren, Y. *et al.* The dynamic interactive network of long non-coding RNAs and chromatin accessibility facilitates erythroid differentiation. *bioRxiv* (2021).

72 Lv, J., Wang, L., Gao, Y., Ding, Y. Q. & Liu, F. 5-hydroxytryptamine synthesized in the aorta-gonad-mesonephros regulates hematopoietic stem and progenitor cell survival. *J Exp Med* **214**, 529-545, doi:10.1084/jem.20150906 (2017).

73 Oberlin, E. *et al.* VE-cadherin expression allows identification of a new class of hematopoietic stem cells within human embryonic liver. *Blood* **116**, 4444-4455, doi:10.1182/blood-2010-03-272625 (2010).

74 Chen, Y., Haviernik, P., Bunting, K. D. & Yang, Y. C. Cited2 is required for normal hematopoiesis in the murine fetal liver. *Blood* **110**, 2889-2898, doi:10.1182/blood-2007-01-066316 (2007).

75 Lancini, C., Gargiulo, G., van den Berk, P. C. & Citterio, E. Quantitative analysis by next generation sequencing of hematopoietic stem and progenitor cells (LSK) and of splenic B cells transcriptomes from wild-type and Usp3-knockout mice. *Data Brief* **6**, 556-561, doi:10.1016/j.dib.2015.12.049 (2016).

76 Zhao, Y. *et al.* ATF4 plays a pivotal role in the development of functional

hematopoietic stem cells in mouse fetal liver. *Blood* **126**, 2383-2391, doi:10.1182/blood-2015-03-633354 (2015).

77 Yu, G., Wang, L. G., Han, Y. & He, Q. Y. clusterProfiler: an R package for comparing biological themes among gene clusters. *OMICS* **16**, 284-287, doi:10.1089/omi.2011.0118 (2012).

Figure Legends

Fig 1. Single-cell transcriptomics atlas of the developing mouse FL. a Schematic diagram of the procedures for tissue processing, cell isolation, and scRNA-seq profiling of FL. HSCs/MPPs, hematopoietic stem cells and multipotent progenitors; ECs, endothelial cells; HCs, hematopoietic cells; NCs, non-hematopoietic/non-endothelial cells. **b** UMAP visualization of all single cells colored by cell clusters in the FL. MegE progenitor, megakaryocytic-erythroid progenitor. **c** Heatmap showing row-scaled expression of the top 20 differentially expressed genes (DEGs, Bonferroni-corrected *P*-values < 0.05, Wilcoxon Rank Sum test) per cluster. **d** Enriched gene ontology (GO) terms in HSCs/MPPs during FL development. **e** Dot plots of the enriched DEGs in HSCs/MPPs during FL development.

Fig 2. CD93-enriched HSCs/MPPs exhibit enhanced stem cell properties. a GO analysis among the three HSC/MPP subtypes. **b** Dot plots of the enriched DEGs in the three HSC/MPP subtypes. **c** Scatter plots of all gene expression in HSC/MPP1 versus HSC/MPP2 (Left) or versus HSC/MPP2 (Right). Differentially expressed transcription factors are colored. **d** Boxplots showing the hscScore distribution in the three HSC/MPP subtypes. Student's t test. **e** Trajectory analysis by PHATE reconstructing the lineage differentiation from HSCs/MPPs to lymphoid, and myeloid progenitors, respectively. **f** Heatmap showing the expression pattern of HSC/MPP signature genes and *Cd93* in the three HSC/MPP subtypes. **g** Donor-derived chimerism in the peripheral blood (PB) of recipients at 8 weeks after primary transplantation using $CD93^{+}$SLAM-LSK ($CD93^{+}$HSC) and $CD93^{-}$HSC. n = 3 biological replicates. **h** Donor-derived chimerism in the PB of recipients at 20 weeks after primary transplantation using

884 $CD93^{+}$HSC and $CD93^{-}$HSC. n = 3 biological replicates. **i** Donor-derived chimerism in the PB
885 of recipients at 8 weeks after secondary transplantation using $CD93^{+}$HSC and $CD93^{-}$HSC. n =
886 3 biological replicates. **j** Donor-derived chimerism in the PB of recipients at 16 weeks after
887 secondary transplantation using $CD93^{+}$HSC and $CD93^{-}$HSC. n = 3 biological replicates. The
888 statistical results are presented as mean ± SEM. Student's t test: *, $P < 0.05$; **, $P < 0.01$.
889
890 **Fig 3. Integration of scRNA-seq and ST decodes cell-cell interactions between**
891 **HSCs/MPPs and niche cells. a** Schematic diagram indicating the cell-cell interaction between
892 HSCs/MPPs and niche cells (Endothelial cells, Stromal cells, Hepatoblasts and Macrophages).
893 **b** CellPhoneDB analysis showing the major HSC/MPP−niche cell interaction pairs. The
894 asterisks mean *P*-value < 0.05 (permutation test) in corresponding cells. EC, endothelial cell,
895 Hep, hepatoblast; SC, stromal cell; Mac, macrophage. **c** Dot plots of the ligand (top) and
896 corresponding receptor (bottom) expression pattern of the major HSC/MPP−niche cell
897 interaction pairs. **d** Schematic diagram of the procedures for 10x Visium Spatial
898 Transcriptomics (ST) experiments. **e** Hematoxylin and eosin (HE) staining of embryonic days
899 (E)14.5 embryo tissue sections (top) included in ST analysis. Sections are shown in the dorsal
900 (Slice 1) to the ventral direction (Slice 4); Tissue sections (middle) and UMAP visualization
901 (bottom) showing unbiased clustering of ST spots. **f** Expression pattern of hepatoblast marker
902 *Afp* in tissue sections. **g** Heatmap showing predicted enrichment scores of spots and two spot
903 patterns of FL. **h** Spatial feature plots of the two spot patterns in FL sections.
904
905 **Fig 4. Identification of expansion units of HSCs/MPPs. a** Schematic diagram indicating the

intra-spots, inter-spots and others. Intra-spots, HSC/MPP-localized spots; Inter-spots, HSC/MPP-surrounded spots; Others, other distant spots. **b** Boxplots showing the enrichment score of niche cells in intra-spots, inter-spots, and others. **c** Boxplots showing the normalized (enrichment) score of niche cells in intra-spots. **d** Boxplots showing the normalized (enrichment) score of niche cells in inter-spots. **e** Co-expression pattern of *Ptn* and *Ptprs* in the FL section. **f** Spatial feature plots of *Ptn-Ptprs* enriched HSC/MPP expansion units. Spatial feature plots showing the expression pattern of ligand gene *Ptn* in niche cells-localized spots (top, red spots), and receptor gene *Ptprs* in HSCs/MPPs-localized spots (top, blue spots). Spatial feature plots showing the cell types in HSC/MPP expansion units (middle). Schematic diagram indicating the *Ptn-Ptprs* enriched HSC/MPP expansion units (bottom). **g** Co-expression pattern of *Mdk* and *Lrp1* in the FL section. **h** Spatial feature plots of the *Mdk-Lrp1* enriched HSC/MPP expansion units (inter-spots). **i** Spatial feature plots of the *Mdk-Lrp1* enriched HSC/MPP expansion units (intra-spots).

Fig 5. Macrophages promoting HSC/MPP expansion. a Immunofluorescence analysis showing the expression of F4/80 (representing macrophages) and c-Kit (representing HSCs/MPPs) in E14.5 FL cryosections. **b** Immunofluorescence analysis showing the expression of F4/80 (representing macrophages), and Runx1 (representing HSCs/MPPs) in E14.5 FL cryosections. **c** The proportion of HSCs/MPPs with and without cellular interaction, respectively (n > 3 biological replicates). **d** Immunofluorescence analysis showing the expression of F4/80 (representing macrophages), CD150 (representing HSCs/MPPs), Mecom (representing HSCs/MPPs) and Hlf (representing HSCs/MPPs) in E14.5 FL cryosections. **e**

928 Schematic diagram of the procedures for HSC/MPP co-culture with macrophages. **f** The
929 number of HSCs/MPPs (LSK cells) derived from macrophage and HSC/MPP co-culture system.
930 Macrophages were combined with half of F4/80^{low} and half of F4/80^{high} macrophages. n = 3
931 biological replicates. **g** The number of HSCs/MPPs (LSK cells) derived from the MDK (50
932 ng/mL)-supplemented culture of 100 HSCs/MPPs (LSK, Flt3^{-}LSK and SLAM-LSK cells). n =
933 3 biological replicates. **h** Total cellularity in E14.5 FL after Clodronate-liposome and Control-
934 liposome treatment. Clodronate-liposome, Clodronate-L; Control-liposome, Control-L, n > 3
935 biological replicates. **i** The proportion of Lineage^{-} (Lin^{-}) cells in E14.5 FL after Clodronate-
936 liposome and Control-liposome treatment, n > 3 biological replicates **j** The proportion of LSK
937 cells in E14.5 FL after Clodronate-liposome and Control-liposome treatment, n > 3 biological
938 replicates. **k** The proportion of SLAM-LSK cells in E14.5 FL after Clodronate-liposome and
939 Control-liposome treatment, n > 3 biological replicates. **l** Flow cytometry analysis showing the
940 proportions of Lin^{-}, LSK, SLAM-LSK cells in E14.5 FL after Clodronate-liposome and
941 Control-liposome treatment. Scale bars, 20 μm. The statistical results are presented as mean ±
942 SEM. Student's t test: *, $P < 0.05$; **, $P < 0.01$.
943
944 **Fig 6. Structure niche cells promoting HSC/MPP expansion. a** Immunofluorescence
945 analysis showing the expression of Lyve1 (representing sinusoid ECs) and Runx1 (representing
946 HSCs/MPPs) in E14.5 FL cryosections. Scale bar, 50 μm. **b** Immunofluorescence analysis
947 showing the expression of Lyve1 (representing sinusoid ECs) and Runx1 (representing
948 HSCs/MPPs) in E14.5 FL cryosections. Scale bar, 50 μm. **c** Immunofluorescence analysis
949 showing the expression of c-Kit (representing HSCs/MPPs), Runx1 (representing HSCs/MPPs),

and EphrinB2 (representing arterial portal vessels) in E14.5 FL cryosections. Yellow arrowheads indicate the c-Kit and Runx1 double-positive HSCs/MPPs. Scale bar, 50 μm. **d** Immunofluorescence analysis showing the expression of c-Kit (representing HSCs/MPPs), Runx1 (representing HSCs/MPPs), and EphB4 (representing veins) in E14.5 FL cryosections. Yellow arrowheads indicate the c-Kit and Runx1 double-positive HSCs/MPPs. Scale bar, 25 μm. **e** Dot plots of the expression patterns of *Igfbp1*, *Igfbp5*, and *Igfbp7* in three structural niche cells (endothelial cell, stromal cell, and hepatoblast). **f** The number of HSCs/MPPs (LSK cells) derived from the factors (50 ng/mL concentration of each factor)-supplemented culture of 100 SLAM-LSK cells from E14.5 FL. n = 3 biological replicates. **g** The number of HSCs/MPPs (LSK cells) derived from the factors (50 ng/mL concentration of each factor)-supplemented culture of 100 Flt3$^-$-LSK cells from E14.5 FL. n = 3 biological replicates. **h** The number of HSCs/MPPs (LSK cells) derived from the factors (50 ng/mL concentration of each factor)-supplemented culture of 100 LSK cells from E14.5 FL. n = 3 biological replicates. The statistical results are presented as mean ± SEM. Student's t test: *, $P < 0.05$; **, $P < 0.01$.

Fig 7. Cross-species analysis of FL hematopoiesis between mice and humans. a UMAP visualization of all cell types in the mouse E14.5 FL. Numbers indicate cell types; each dot represents one cell. **b** UMAP visualization of the FL cell populations from mice (E14.5) and humans (11 post-conception weeks). Yellow indicates the mouse cell population and blue indicates the human cell population. **c** GO analysis of the top DEGs related to biological processes in human HSCs/MPPs. **d** GO analysis of the top DEGs related to biological processes in mouse HSCs/MPPs. **e** Ligand-receptor interaction network showing the potential

communications between human HSCs/MPPs and niche cells. **f** Heatmap showing the major human HSC/MPP-niche cell interaction pairs. The asterisks mean *P*-value < 0.05 (permutation test) in corresponding cells. **g-h** Immunofluorescence analysis showing the expression of CD68 (representing macrophages) and CD34 (representing HSCs/MPPs) in human 11 post-conception week FL section. Scale bars, 20 μm. **i** The proportion of HSCs/MPPs with and without cellular interaction, respectively (n > 3 biological replicates). **j** The number of human $CD34^+$HSCs/MPPs derived from mouse macrophage and HSC/MPP co-culture system. The statistical data are the cell number of $CD34^+$ cells (total number of co-culture cells × the proportion of $CD34^+$ cells in total co-cultured cells) after co-culture. $F4/80^{low}$ macrophages were $CD45^+CD11b^+F4/80^{low}$ macrophages, $F4/80^{high}$ macrophages were $CD45^+CD11b^{low}F4/80^{high}$ macrophages, macrophages were combined with half of $F4/80^{low}$ and half of $F4/80^{high}$ macrophages. n > 3 biological replicates. The statistical results are presented as mean ± SEM. Student's t test: *, $P < 0.05$; **, $P < 0.01$; ***, $P < 0.001$.

Fig. 1

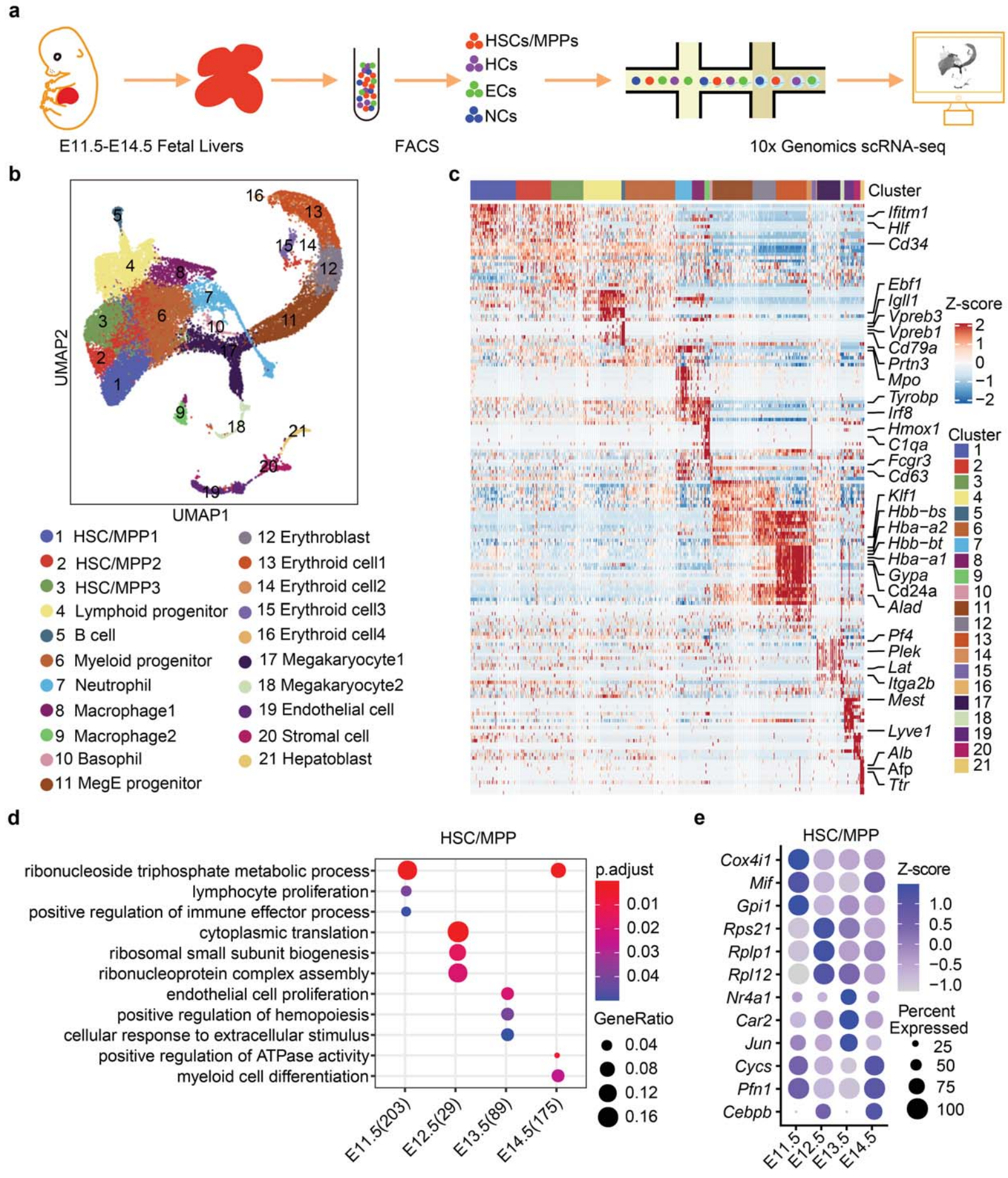
a
HSCs/MPPs
HCs
ECs
NCs
E11.5-E14.5 Fetal Livers
FACS
10x Genomics scRNA-seq
b
UMAP1
UMAP2
1 HSC/MPP1
2 HSC/MPP2
3 HSC/MPP3
4 Lymphoid progenitor
5 B cell
6 Myeloid progenitor
7 Neutrophil
8 Macrophage1
9 Macrophage2
10 Basophil
11 MegE progenitor
12 Erythroblast
13 Erythroid cell1
14 Erythroid cell2
15 Erythroid cell3
16 Erythroid cell4
17 Megakaryocyte1
18 Megakaryocyte2
19 Endothelial cell
20 Stromal cell
21 Hepatoblast
c
Cluster
Ifitm1
Hlf
Cd34
Ebf1
Igll1
Vpreb3
Vpreb1
Cd79a
Prtn3
Mpo
Tyrobp
Irf8
Hmox1
C1qa
Fcgr3
Cd63
Klf1
Hbb-bs
Hba-a2
Hbb-bt
Hba-a1
Gypa
Cd24a
Alad
Pf4
Plek
Lat
Itga2b
Mest
Lyve1
Alb
Afp
Ttr
Z-score
d
HSC/MPP
ribonucleoside triphosphate metabolic process
lymphocyte proliferation
positive regulation of immune effector process
cytoplasmic translation
ribosomal small subunit biogenesis
ribonucleoprotein complex assembly
endothelial cell proliferation
positive regulation of hemopoiesis
cellular response to extracellular stimulus
positive regulation of ATPase activity
myeloid cell differentiation
E11.5(203)
E12.5(29)
E13.5(89)
E14.5(175)
p.adjust
GeneRatio
e
HSC/MPP
Cox4i1
Mif
Gpi1
Rps21
Rplp1
Rpl12
Nr4a1
Car2
Jun
Cycs
Pfn1
Cebpb
E11.5
E12.5
E13.5
E14.5
Z-score
Percent Expressed

Fig. 2

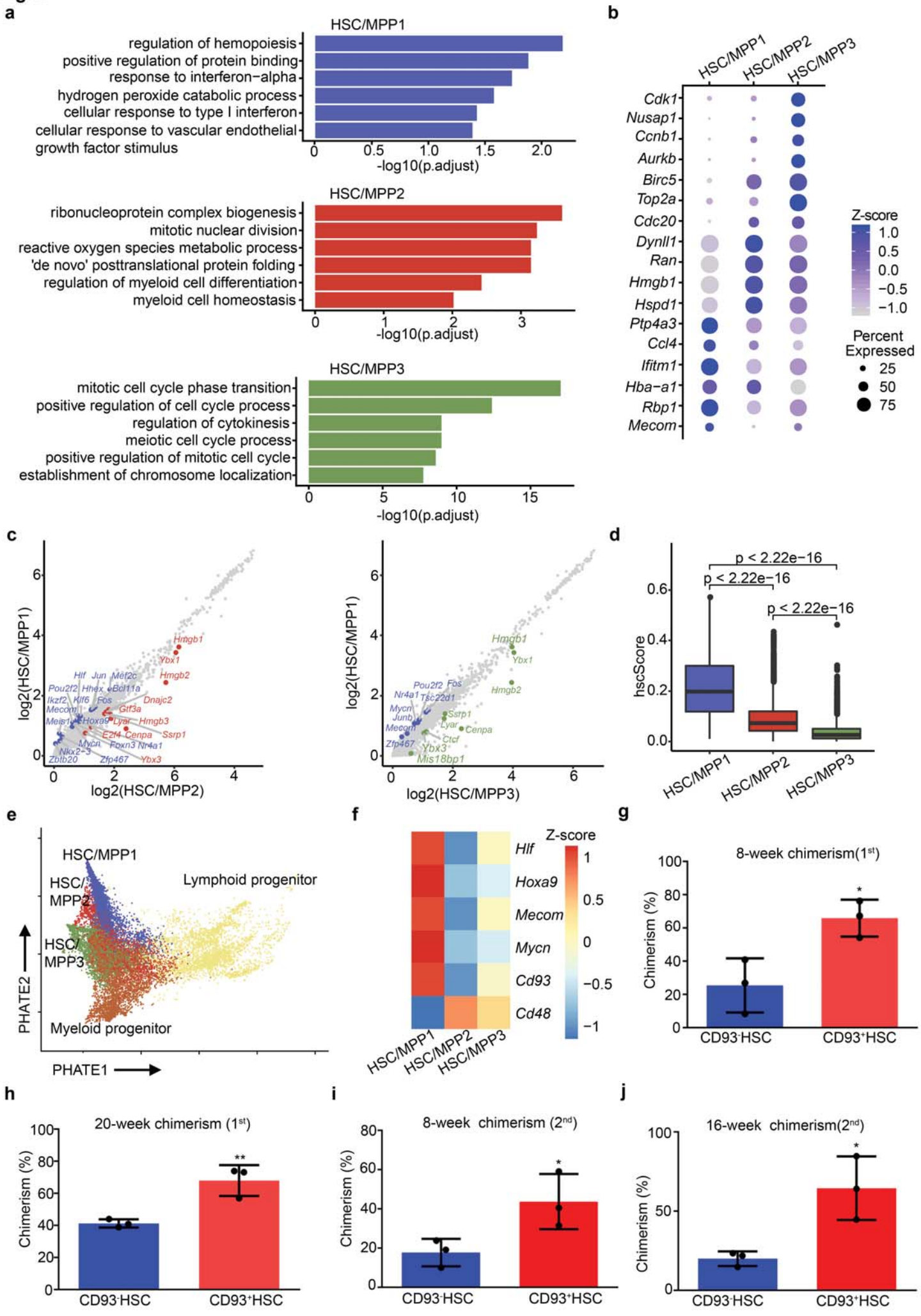
a
HSC/MPP1
regulation of hemopoiesis
positive regulation of protein binding
response to interferon−alpha
hydrogen peroxide catabolic process
cellular response to type I interferon
cellular response to vascular endothelial growth factor stimulus
-log10(p.adjust)
HSC/MPP2
ribonucleoprotein complex biogenesis
mitotic nuclear division
reactive oxygen species metabolic process
'de novo' posttranslational protein folding
regulation of myeloid cell differentiation
myeloid cell homeostasis
-log10(p.adjust)
HSC/MPP3
mitotic cell cycle phase transition
positive regulation of cell cycle process
regulation of cytokinesis
meiotic cell cycle process
positive regulation of mitotic cell cycle
establishment of chromosome localization
-log10(p.adjust)
b
HSC/MPP1
HSC/MPP2
HSC/MPP3
Cdk1
Nusap1
Ccnb1
Aurkb
Birc5
Top2a
Cdc20
Dynll1
Ran
Hmgb1
Hspd1
Ptp4a3
Ccl4
Ifitm1
Hba−a1
Rbp1
Mecom
Z-score
Percent Expressed
c
log2(HSC/MPP1)
log2(HSC/MPP2)
log2(HSC/MPP3)
d
hscScore
p < 2.22e−16
HSC/MPP1
HSC/MPP2
HSC/MPP3
e
HSC/MPP1
HSC/MPP2
HSC/MPP3
Lymphoid progenitor
Myeloid progenitor
PHATE1
PHATE2
f
Z-score
Hlf
Hoxa9
Mecom
Mycn
Cd93
Cd48
HSC/MPP1
HSC/MPP2
HSC/MPP3
g
8-week chimerism(1st)
Chimerism (%)
CD93-HSC
CD93+HSC
h
20-week chimerism (1st)
Chimerism (%)
CD93-HSC
CD93+HSC
i
8-week chimerism (2nd)
Chimerism (%)
CD93-HSC
CD93+HSC
j
16-week chimerism(2nd)
Chimerism (%)
CD93-HSC
CD93+HSC

Fig. 3

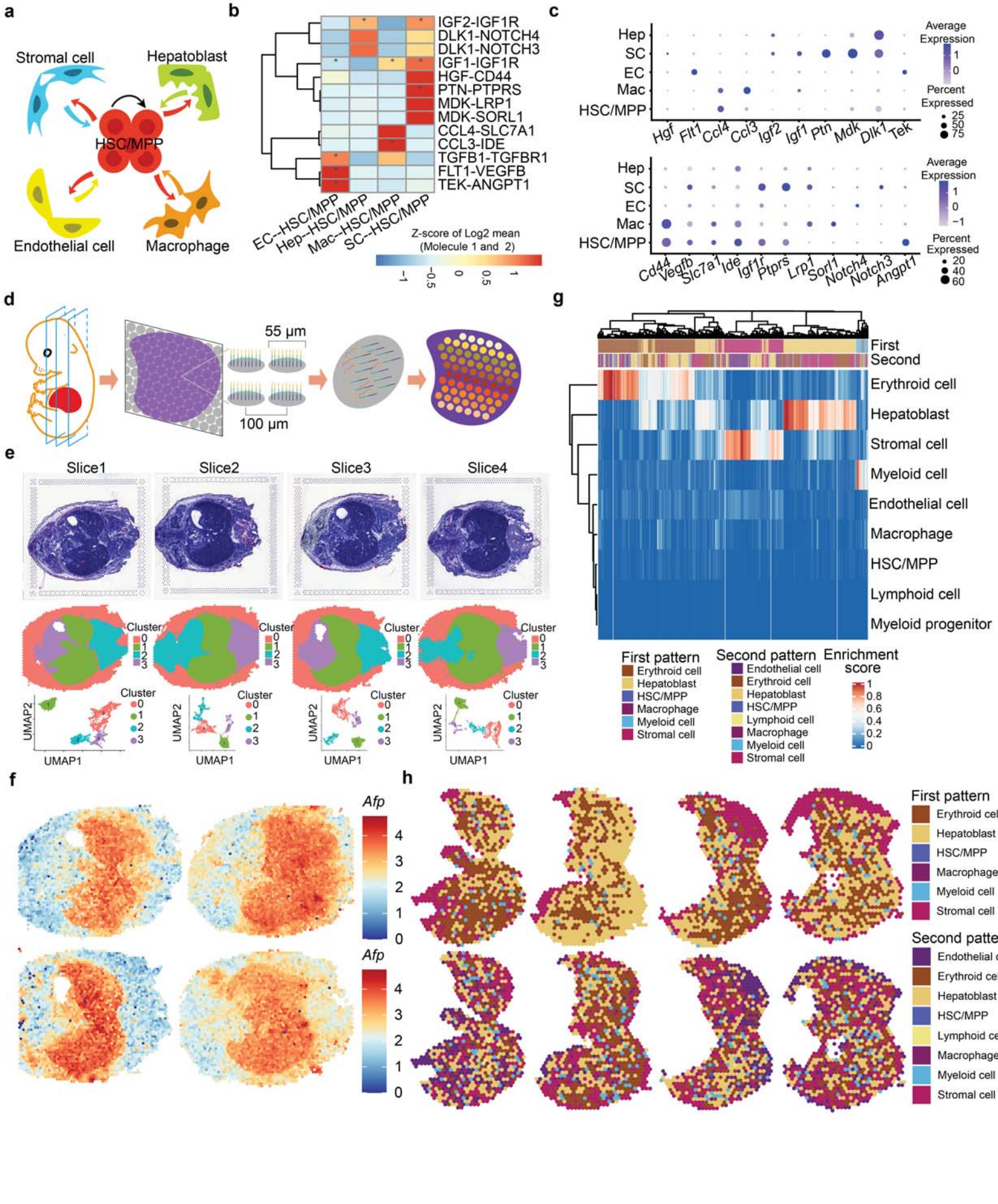
a
Stromal cell
Hepatoblast
HSC/MPP
Endothelial cell
Macrophage
b
IGF2-IGF1R
DLK1-NOTCH4
DLK1-NOTCH3
IGF1-IGF1R
HGF-CD44
PTN-PTPRS
MDK-LRP1
MDK-SORL1
CCL4-SLC7A1
CCL3-IDE
TGFB1-TGFBR1
FLT1-VEGFB
TEK-ANGPT1
EC--HSC/MPP
Hep--HSC/MPP
Mac--HSC/MPP
SC--HSC/MPP
Z-score of Log2 mean (Molecule 1 and 2)
c
Hep
SC
EC
Mac
HSC/MPP
Hgf
Flt1
Ccl4
Ccl3
Igf2
Igf1
Ptn
Mdk
Dlk1
Tek
Average Expression
Percent Expressed
Cd44
Vegfb
Slc7a1
Ide
Igf1r
Ptprs
Lrp1
Sorl1
Notch4
Notch3
Angpt1
d
55 μm
100 μm
e
Slice1
Slice2
Slice3
Slice4
Cluster
UMAP1
UMAP2
g
First
Second
Erythroid cell
Hepatoblast
Stromal cell
Myeloid cell
Endothelial cell
Macrophage
HSC/MPP
Lymphoid cell
Myeloid progenitor
First pattern
Second pattern
Enrichment score
f
Afp
h
First pattern
Second pattern

Fig. 4

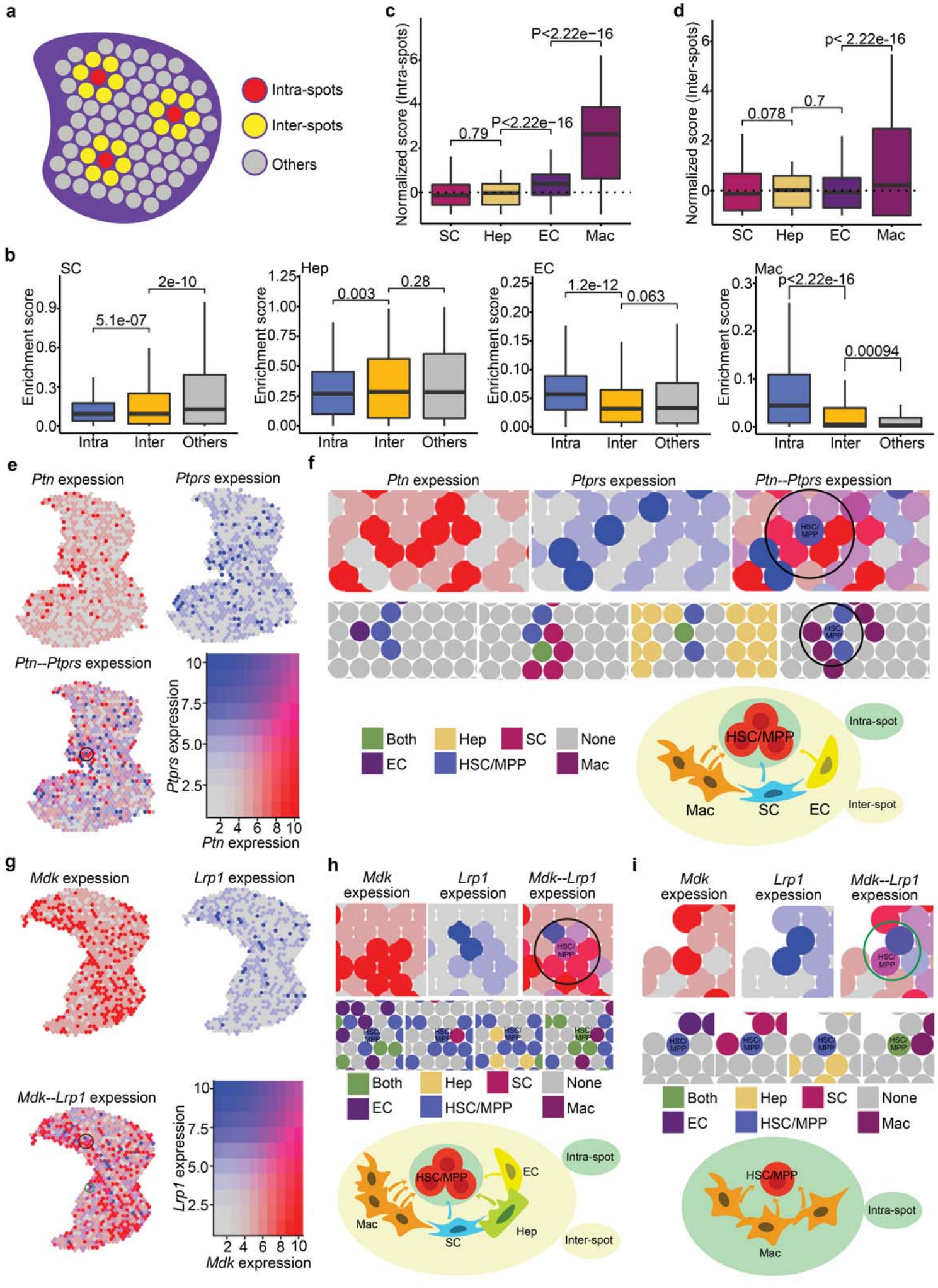
a
Intra-spots
Inter-spots
Others
c
Normalized score (Intra-spots)
P<2.22e−16
0.79
P<2.22e−16
SC
Hep
EC
Mac
d
Normalized score (Inter-spots)
p< 2.22e-16
0.078
0.7
SC
Hep
EC
Mac
b
SC
Enrichment score
5.1e-07
2e-10
Intra
Inter
Others
Hep
0.003
0.28
EC
1.2e-12
0.063
Mac
p<2.22e-16
0.00094
e
Ptn expression
Ptprs expression
Ptn--Ptprs expression
Ptprs expression
Ptn expression
f
Ptn expression
Ptprs expression
Ptn--Ptprs expression
HSC/MPP
Both
Hep
SC
None
EC
HSC/MPP
Mac
Intra-spot
Inter-spot
Mac
SC
EC
g
Mdk expression
Lrp1 expression
Mdk--Lrp1 expression
Lrp1 expression
Mdk expression
h
Mdk expression
Lrp1 expression
Mdk--Lrp1 expression
HSC/MPP
Both
Hep
SC
None
EC
HSC/MPP
Mac
Intra-spot
Inter-spot
Mac
SC
Hep
EC
i
Mdk expression
Lrp1 expression
Mdk--Lrp1 expression
HSC/MPP
Both
Hep
SC
None
EC
HSC/MPP
Mac
Intra-spot
HSC/MPP
Mac

Fig. 5

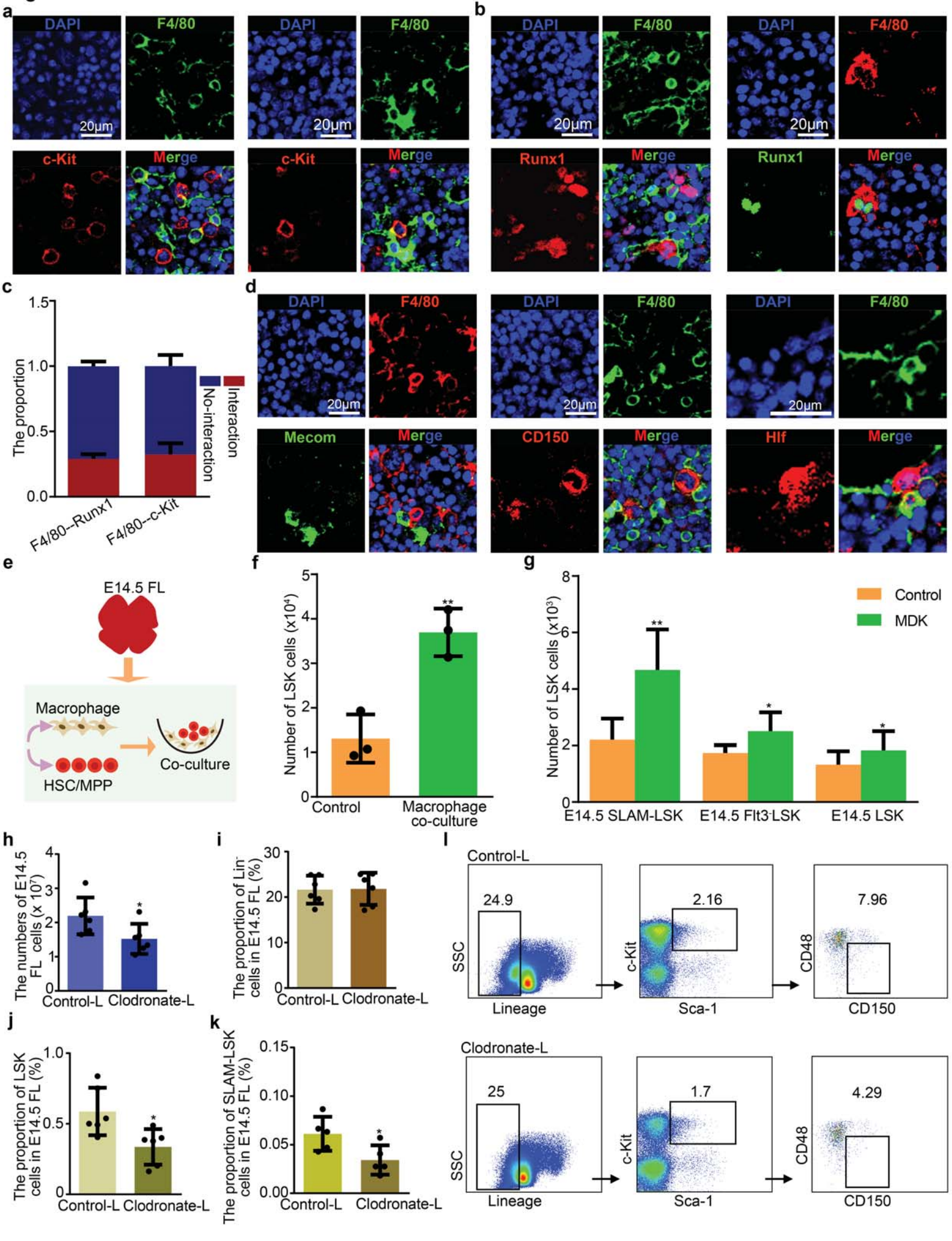
a
DAPI
F4/80
20μm
c-Kit
Merge
b
Runx1
c
The proportion
No-interaction
Interaction
F4/80--Runx1
F4/80--c-Kit
d
Mecom
CD150
Hlf
e
E14.5 FL
Macrophage
HSC/MPP
Co-culture
f
Number of LSK cells (x10⁴)
Control
Macrophage co-culture
g
Number of LSK cells (x10³)
Control
MDK
E14.5 SLAM-LSK
E14.5 Flt3⁻LSK
E14.5 LSK
h
The numbers of E14.5 FL cells (x 10⁷)
Control-L
Clodronate-L
i
The proportion of Lin⁻ cells in E14.5 FL (%)
l
Control-L
24.9
2.16
7.96
SSC
Lineage
c-Kit
Sca-1
CD48
CD150
j
The proportion of LSK cells in E14.5 FL (%)
k
The proportion of SLAM-LSK cells in E14.5 FL (%)
Clodronate-L
25
1.7
4.29

Fig. 6

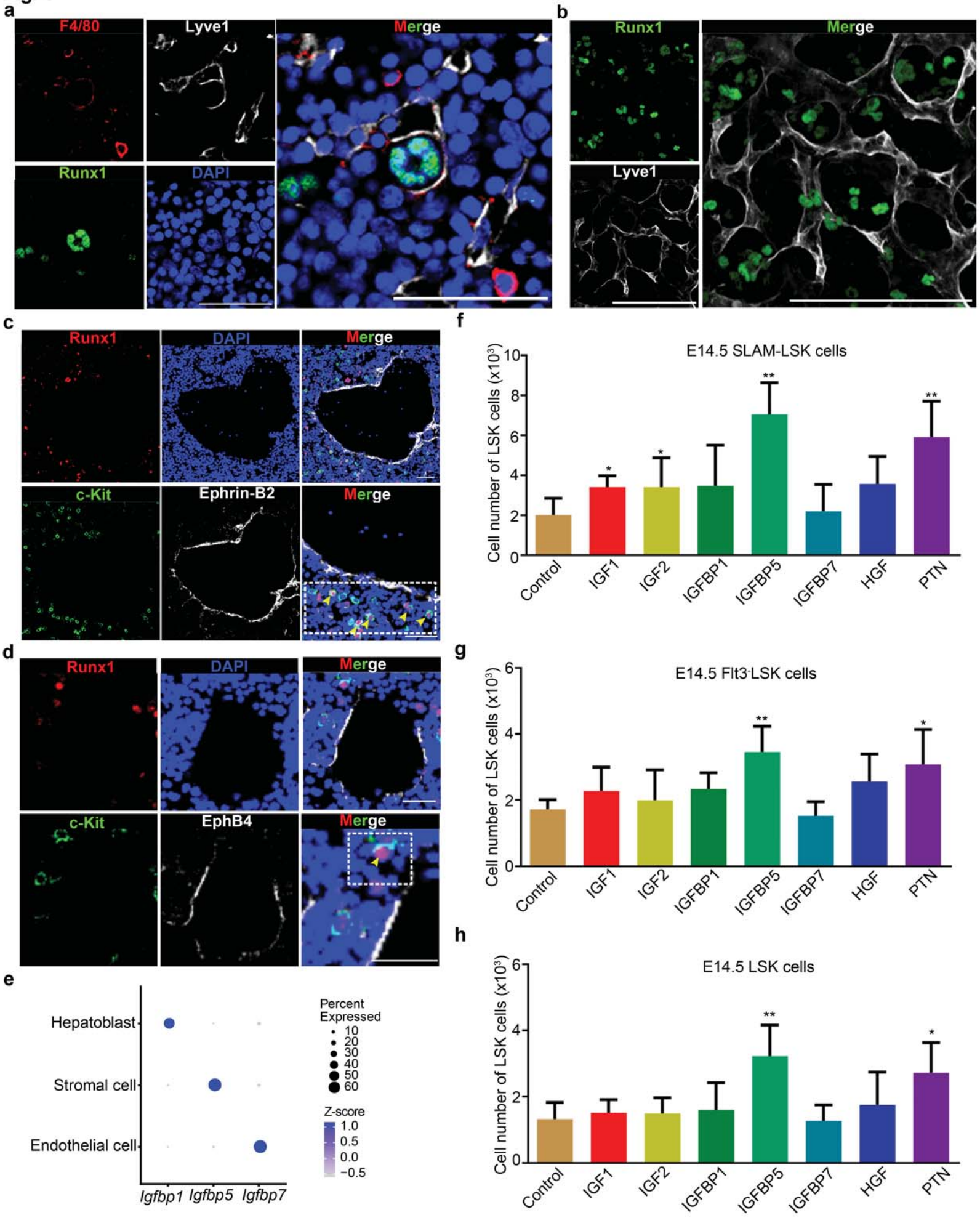
a
F4/80
Lyve1
Merge
Runx1
DAPI
b
Runx1
Merge
Lyve1
c
Runx1
DAPI
Merge
c-Kit
Ephrin-B2
Merge
d
Runx1
DAPI
Merge
c-Kit
EphB4
Merge
e
Hepatoblast
Stromal cell
Endothelial cell
Igfbp1 Igfbp5 Igfbp7
Percent Expressed
10
20
30
40
50
60
Z-score
1.0
0.5
0.0
−0.5
f
E14.5 SLAM-LSK cells
Cell number of LSK cells (x10³)
Control
IGF1
IGF2
IGFBP1
IGFBP5
IGFBP7
HGF
PTN
g
E14.5 Flt3⁻LSK cells
Cell number of LSK cells (x10³)
h
E14.5 LSK cells
Cell number of LSK cells (x10³)

Fig. 7

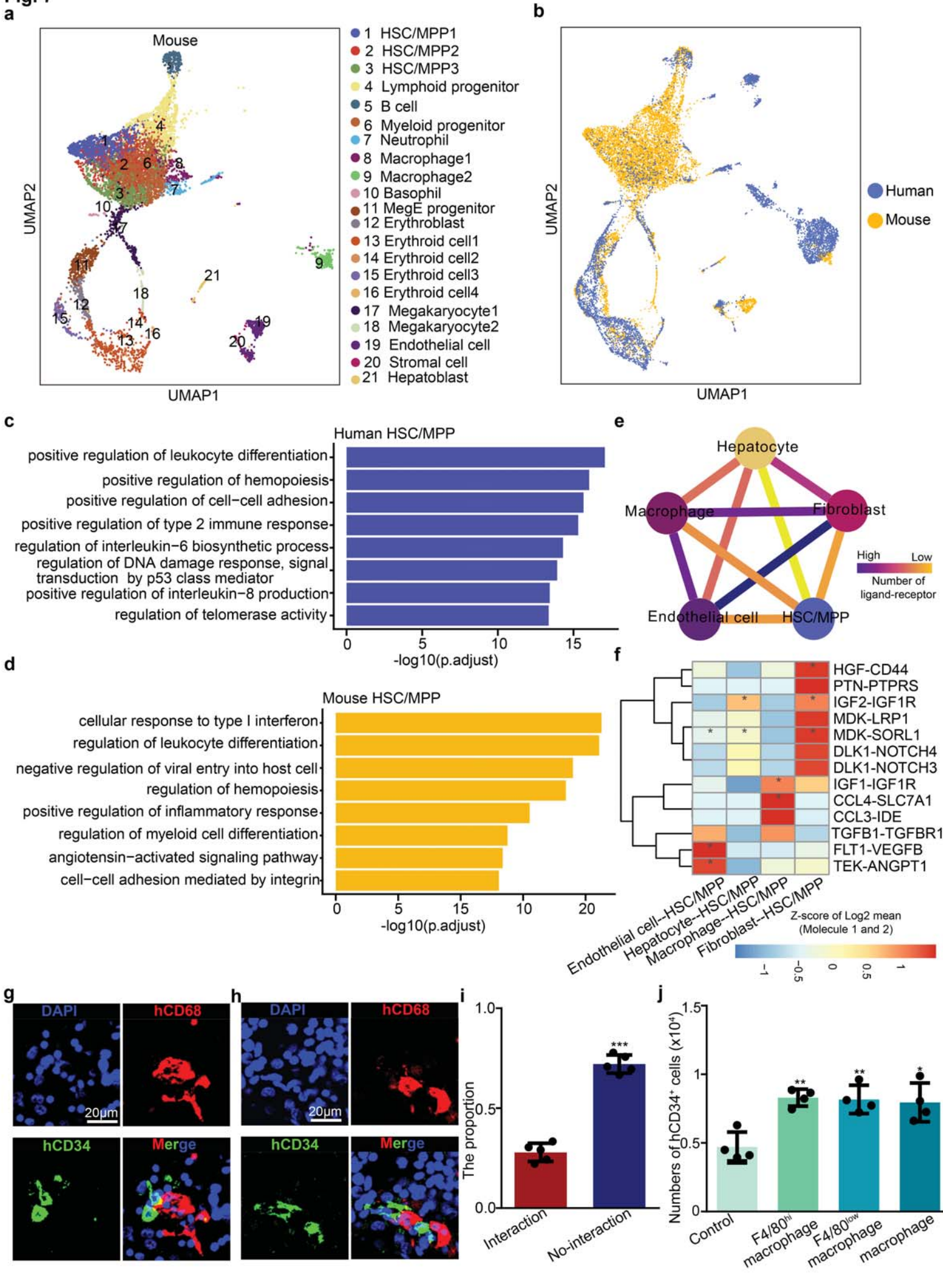
a
Mouse
UMAP2
UMAP1
1 HSC/MPP1
2 HSC/MPP2
3 HSC/MPP3
4 Lymphoid progenitor
5 B cell
6 Myeloid progenitor
7 Neutrophil
8 Macrophage1
9 Macrophage2
10 Basophil
11 MegE progenitor
12 Erythroblast
13 Erythroid cell1
14 Erythroid cell2
15 Erythroid cell3
16 Erythroid cell4
17 Megakaryocyte1
18 Megakaryocyte2
19 Endothelial cell
20 Stromal cell
21 Hepatoblast
b
UMAP2
UMAP1
Human
Mouse
c
Human HSC/MPP
positive regulation of leukocyte differentiation
positive regulation of hemopoiesis
positive regulation of cell−cell adhesion
positive regulation of type 2 immune response
regulation of interleukin−6 biosynthetic process
regulation of DNA damage response, signal transduction by p53 class mediator
positive regulation of interleukin−8 production
regulation of telomerase activity
-log10(p.adjust)
d
Mouse HSC/MPP
cellular response to type I interferon
regulation of leukocyte differentiation
negative regulation of viral entry into host cell
regulation of hemopoiesis
positive regulation of inflammatory response
regulation of myeloid cell differentiation
angiotensin−activated signaling pathway
cell−cell adhesion mediated by integrin
-log10(p.adjust)
e
Hepatocyte
Macrophage
Fibroblast
Endothelial cell
HSC/MPP
High
Low
Number of ligand-receptor
f
HGF-CD44
PTN-PTPRS
IGF2-IGF1R
MDK-LRP1
MDK-SORL1
DLK1-NOTCH4
DLK1-NOTCH3
IGF1-IGF1R
CCL4-SLC7A1
CCL3-IDE
TGFB1-TGFBR1
FLT1-VEGFB
TEK-ANGPT1
Endothelial cell–HSC/MPP
Hepatocyte–HSC/MPP
Macrophage–HSC/MPP
Fibroblast–HSC/MPP
Z-score of Log2 mean (Molecule 1 and 2)
g
DAPI
hCD68
hCD34
Merge
20μm
h
DAPI
hCD68
hCD34
Merge
20μm
i
The proportion
Interaction
No-interaction
j
Numbers of hCD34+ cells (x10^4)
Control
F4/80hi macrophage
F4/80low macrophage
macrophage